Methodology for Determining Electronic Transference Numbers in Molten Sulfide Melts

by

Jaclyn L. Cann

B.S., Georgia Institute of Technology (2014)

Submitted to the Department of Materials Science and Engineering
in partial fulfillment of the requirements for the degree of

Master of Science in Materials Science and Engineering

at the

MASSACHUSETTS INSTITUTE OF TECHNOLOGY

June 2017

Author . . . .
Department of Materials Science and Engineering
May 9, 2017

Certified by . . . .
Antoine Allanore
Assistant Professor
Thesis Supervisor

Accepted by . . . .
Donald R. Sadoway
Chairman, Department Committee on Graduate Theses

Methodology for Determining Electronic Transference Numbers in Molten Sulfide Melts

by

Jaclyn L. Cann

Submitted to the Department of Materials Science and Engineering
on May 9, 2017, in partial fulfillment of the
requirements for the degree of
Master of Science in Materials Science and Engineering

Abstract

Electrolysis of molten copper (I) sulfide (Cu_2S) in a sulfide-based electrolyte is being investigated for use as a direct path for copper extraction to replace the conventional process of smelting and electrorefining [1]. The allure of an electrolysis process for metals extraction can be enhanced by increasing its faradaic efficiency, through, for example, decreasing the electronic transference number of the electrolyte. This thesis compares two methods of determining the electronic transference number in Cu_2S - barium sulfide (BaS) electrolytes to determine whether one or both methods are well-suited for use with these high-temperature electrolytes. The first method is a stepped potential chronoamperometry method, in which the electronic transference number is determined from the decay of the current after a voltage step. The second method is a faradaic efficiency method, where the ionic transference number is determined from the efficiency with which ions can be transported from one electrode to the other. The stepped potential chronoamperometry method estimates electronic transference numbers between 0.73 and 0.85, while the faradaic efficiency method estimates values between 0.12 and 0.34 for the same electrolyte. Three differences between the experiments are investigated: (1) the work functions of the electrodes used, (2) the additional alloying driving force in faradaic efficiency experiments, and (3) the tin impurities in the electrolyte. This analysis suggests that the difference between the work function of the electrode and the electron affinity of the electrolyte may be the dominant cause of the experimental discrepancy. Therefore, it is suggested that electrodes and electrolytes be chosen to maximize this difference to enhance the faradaic efficiency of copper extraction from Cu_2S. The underlying physics of semiconductiviy in molten sulfides, however, remains unclear. Future study of the electronic structure and short range ordering of molten metal sulfides to better understand and predict electronic properties is needed.

Thesis Supervisor: Antoine Allanore
Title: Assistant Professor

Acknowledgments

I would like to thank my amazing lab mates, past and present, for their help, discussion, and friendship. Without them, this work would not have been so enriching and enjoyable.

I would like to thank Prof. Allanore for his vision, support, patience, and guidance. I have learned more under his tutelage than I could have ever expected, from learning more about myself and my project to how ideas can be enacted and how change is made.

Thanks also Prof. Lechtman for her help in teaching me to polish and for teaching me to give attention to detail and to have patience.

Thanks to my friends for all the fun! Their support, advice, and jokes are always appreciated, and they make this whole experience a happier one.

Thank you especially to my family (and my second family, the Swifts). They are my foundation, and I wouldn't be the person I am today without them.

Last but not least, thank you to Lance. He is always there for me, and he makes every day brighter. I'm so glad to have him by my side.

Contents

List of Figures

List of Tables

Chapter 1

Introduction

1.1 Motivation

85% of the world's copper supply can be found in the Earth's crust in the form of sulfide ore [2]. The conventional copper extraction method involves smelting and electrorefining steps and is accompanied by the release of sulfur dioxide (SO_2), a harmful air pollutant that can be toxic to humans [2]. SO_2 is then captured to form sulfuric acid (H_2SO_4) as a byproduct of copper smelting [3]. Electrolysis of molten copper (I) sulfide (Cu_2S) in a sulfide electrolyte is being investigated as an alternative, direct path for copper extraction, which would eliminate the production of SO_2 that accompanies the conventional method [1]. Candidate sulfide electrolytes are selected for their stability at high temperatures and for their transport properties. Cu_2S undergoes a semiconductor-semiconductor transition upon melting at 1130°C [4] and is more effective conducting electrons than ions. In order to increase the flux of ions through the electrolyte, which is necessary for higher efficiencies during electrolysis, barium sulfide (BaS) has been proposed as a key compound to form a BaS-Cu_2S electrolyte [1].

The motivation for the present work is the further improvement of the faradaic efficiency obtainable during the electrolysis of Cu_2S. The electrolysis process can be optimized by adjusting the composition of the electrolyte and by choosing appropriate operating conditions, such as temperature and applied voltage. To determine the effect that these changes have on the ionic flux (J_i) and electronic flux (J_e) in the electrolyte, the ionic and electronic transference numbers, t_i and t_e must be determined. t_i and t_e are defined in Equations 1.1 and 1.2, respectively, where J_{total} is the total flux, I_i is the ionic current, I_e is the electronic current, and I_{total} is the total current [5].

$$t_i = \frac{J_i}{J_{total}} = \frac{I_i}{I_{total}} \tag{1.1}$$

$$t_e = \frac{J_e}{J_{total}} = \frac{I_e}{I_{total}} \tag{1.2}$$

There is no established best practice for measuring t_i and t_e in molten metal sulfide electrolytes. The finer details about their physical and electronic structures have yet to be determined. Thus, choosing a method to determine the t_i and t_e and verifying that it is appropriate are difficult, but very necessary tasks.

1.2 Electronic Transference Number Estimation Techniques

Multiple methods have been developed to estimate electronic and ionic transference numbers in materials with mixed ionic and electronic conductivity. We will discuss the Tubandt method, DC residual potential technique, and stepped potential chronoamperometry method. Most of these methods were originally applied to solid materials, but examples will also be presented for molten materials.

When the Tubandt method is applied to materials of mixed conductivity, such a Ag_2S [6] or Cu_2S-CuCl melts [7], a potential is applied between two electrodes across an electrolyte, and the resulting anodic mass loss and cathodic mass gain are used to determine t_i. t_i can be calculated using Equation 1.3, where Δw is the measured mass change of an electrode, $\Delta w_{expected}$ is the mass change predicted using Faraday's law, z is the charge number, F is Faraday's constant, Q is the charge passed, and M_i is the molar mass of the transported ion.

$$t_i = \frac{\Delta w}{\Delta w_{expected}} = \frac{zF\Delta w}{QM_i} \tag{1.3}$$

The DC residual potential technique has been used to study electronic and ionic transference numbers in mixed conductors [8, 9, 10]. In this method, a current step is applied, and the steady state voltage after the current step is compared to the voltage immediately after the current is interrupted in order to determine t_i. Endo [8] measured the ionic and electronic conductivities of molten Ag_2S with this method, with an estimated t_i of < 0.03, which can be compared those of solid Ag_2S at about 0.02 for the α phase and 0.35 for the β phase [9]. Yokota [11] examined electrode type (ionic or electronic) and its effect on measurements both experimentally and theoretically.

The stepped potential chronoamperometry method developed by Fried [5] is cousin to the DC residual potential method. Instead of analyzing the relaxation of potential after a current step is interrupted, it analyzes the relaxation of current after a potential step (see Section 2.3). Fried used this method for molten TiO_2-BaO of varying composition and temperature and found that at 1400 °C when the BaO concentration was increased from 27 mol% to 33 mol% t_i increased from 0.106 to 0.167, a change that was repeatable at other temperatures.

1.3 Molten Semiconductors

In 1952, Guggenheim wrote that "... it is useful, even through untrue, to treat a liquid as if the molecules were arranged on a lattice" [12]. Even today, assumptions about the properties of liquids are often made based on the properties that those materials exhibit as solids, and models for properties of liquids are often empirical. As such, high temperature experimental data can be unsubstantial. We shall present some of the theories on the electronic behavior of molten semiconductors and known properties of the materials used in the electrolyte in this study, Cu_2S and BaS.

In molten semiconductors, the long-range order on which solid-state band theory is derived is removed. However, after melting of semiconducting compounds, the remaining short-range order allows interpretation using similar concepts [13]. A key difference is that there is no longer a "true" band gap of forbidden states, but rather a pseudogap, where there is a minimum in the density of states.

Figure 1-1a shows the change in behavior of the pseudogap with off-stoichiometry. The pseudogap is deepest at stoichiometry, and the Fermi energy shifts as composition is changed. This is because the pseudogap is a result of the coordination between between the cations and anions, and off-stoichiometry affects that coordination. Increasing temperature also causes the pseudogap to become more shallow, as shown in Figure 1-1b [14]. As molten semiconductors increase in temperature, they are theorized to metallize, passing through a semimetallic transition.

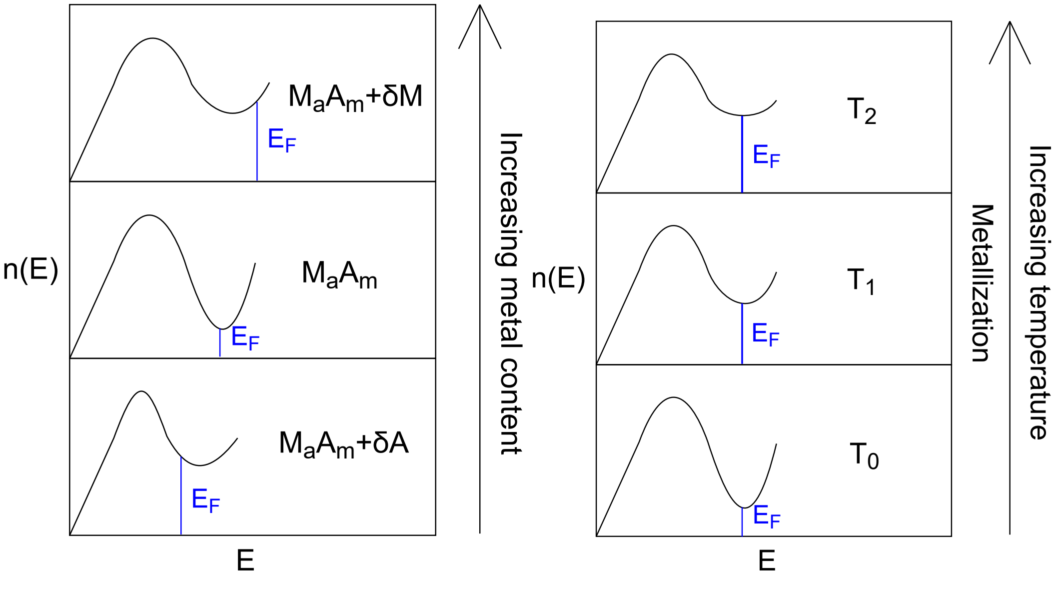

(a) (b)

Figure 1-1: Schematic representation of the (a) composition dependence and (b) temperature dependence of the density of states as a function of energy for semimetallic alloys close to stoichiometry

The structure of molten metal sulfides and its evolution with temperature is important as it affects the electronic behavior. Viscosity, density, ultrasound wave velocity, Hall effect [15], radial distribution functions, and coordination numbers[14] are used to describe structural change. However, such a description has not yet led to band structure calculations mimicking those from solid-state. Instead, we must rely on qualitative observations, such as the variation of kinematic viscosity from exponential behavior with temperature [15], to determine at what temperature significant structural change has occurred and, concurrently, at what temperature a change in electronic behavior can be anticipated.

1.3.1 Properties of Molten Cu_2S and BaS

Figure 1-2 shows a phase diagram for the Cu-S binary system, where a miscibility gap on both sides of the Cu_2S compound indicates that Cu_2S undergoes a semiconductor-semiconductor transition upon melting [16]. The conductivity of Cu_2S increases upon melting and continues to increase as the temperature is increased. In addition, the Seebeck coefficient of Cu_2S is positive before and after melting, indicating that it will exhibit p-type behavior. The density of Cu_2S has also been investigated across melting and has been found to decrease [4]. The enthalpy of melting, the variation of specific heat as a function of temperature, the variation of vapor pressure sulfur above the liquid as a function of temperature, and activation energy for conduction have also been measured [4].

There is less data on molten BaS. The Ba-S phase diagram is incomplete, as shown in Figure 1-3, and the melting point of BaS is not even agreed upon. The electronic properties of solid BaS have been measured up to 1200K, and it has been determined that BaS behaves as an n-type semiconductor [18].

The phase diagram for BaS-Cu_2S is presented in Figure 1-4. It should be noted that the accuracy of the BaS-rich side of the phase diagram is in doubt.

1.4 Electrode-Electrolyte Interfaces

The molten electrolyte itself is not the only component of the experimental methods used to determine transference numbers. Each experimental configuration (see sections 2.3.1 and 2.4.1) has the molten electrolyte in contact with electrodes, either graphite or solid copper and liquid copper-tin, and the interface between the semiconductive electrolyte and those electrodes has an impact on electrical measurements that is important to understand.

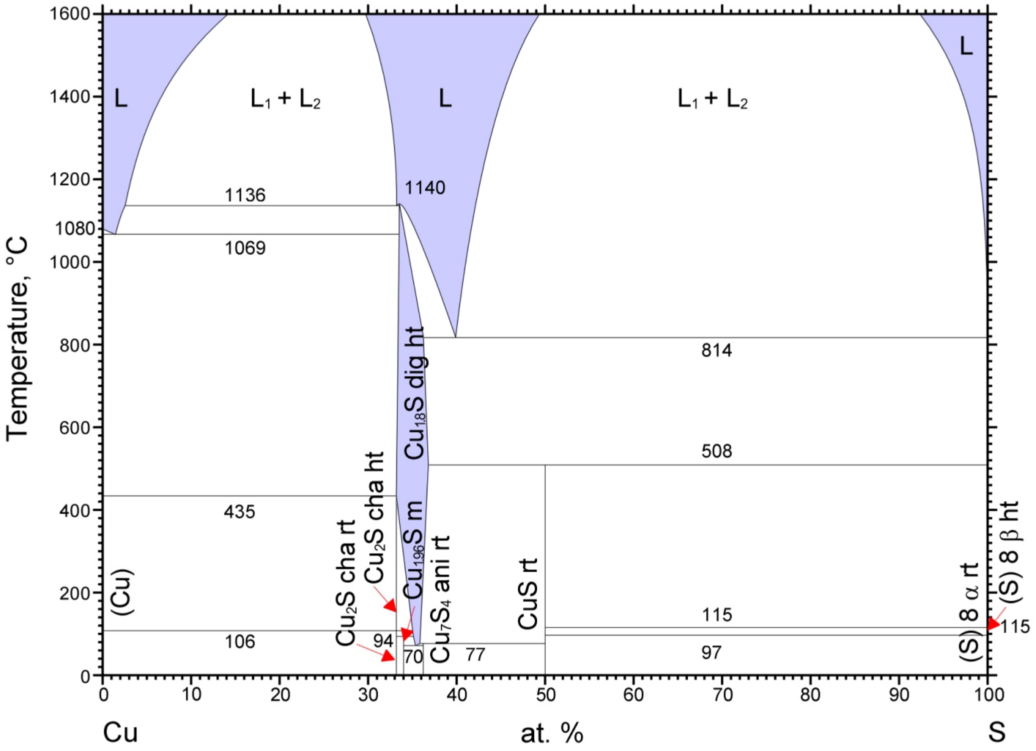

© ASM International 2010. Diagram No. 103258

Figure 1-2: Cu-S phase diagram [17]

At equilibrium, the Fermi levels between materials in electrical contact must match [21]. The contact potential between two metals can be estimated by calculating the difference between their work functions [13]. This is complicated by the uncertainty associated with the work functions themselves. The work function is typically measured on clean ideal surfaces, but the contact surfaces of materials are not consistently clean and ideal; surface orientation may be inconsistent, and surface atoms rearrange.

Figure 1-5a shows the Schottky barrier that forms when a metal and semiconductor are in contact. According to this simple picture, the Schottky barrier (Φ_{SB}) at equilibrium can be calculated from the band gap of the semiconductor (E_g) and the difference between the metal work function (Φ_M) and the semiconductor electron affinity (χ_{SM}), according to Equation 1.4 [22].

$$\Phi_{SB} = E_g - (\Phi_M - \chi_{SC}) \tag{1.4}$$

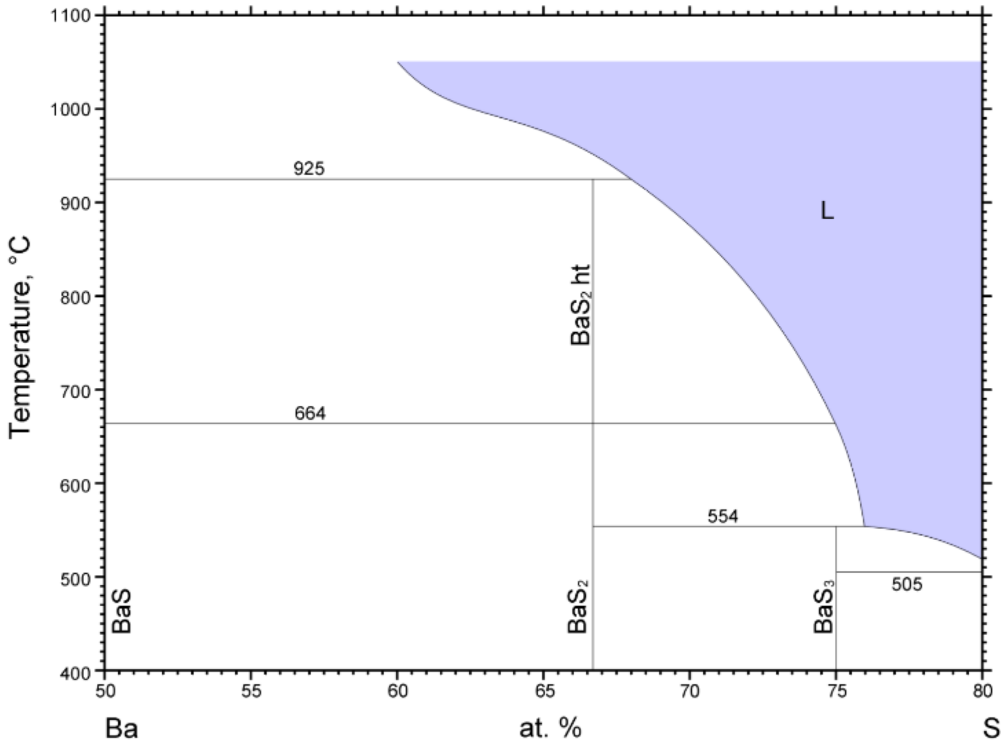

© ASM International 2006. Diagram No. 900370

Figure 1-3: Ba-S phase diagram [19]

Reality is not this simple, however. In addition to complications from uncertainty of the work function and electron affinity, the metal-semiconductor interface is further complicated by chemical bonds between the metal and the semiconductive electrolyte, creating dipoles. When the interfacial states are sufficiently dense, the Fermi level is pinned to the Fermi level of the interface states. The work function of the metal will not change the degree of band bending and will be accomodated through a potential change in the space charge layer (Δ), as shown in Figure 1-5b [22]. The height of the Schottky barrier when interface states are present can be calculated by using Equation 1.5.

$$\Phi_{SB} = E_g - (\Phi_M + \Delta - \chi_{SC}) \tag{1.5}$$

When the interface states are not sufficiently dense, the band edge is pinned. In

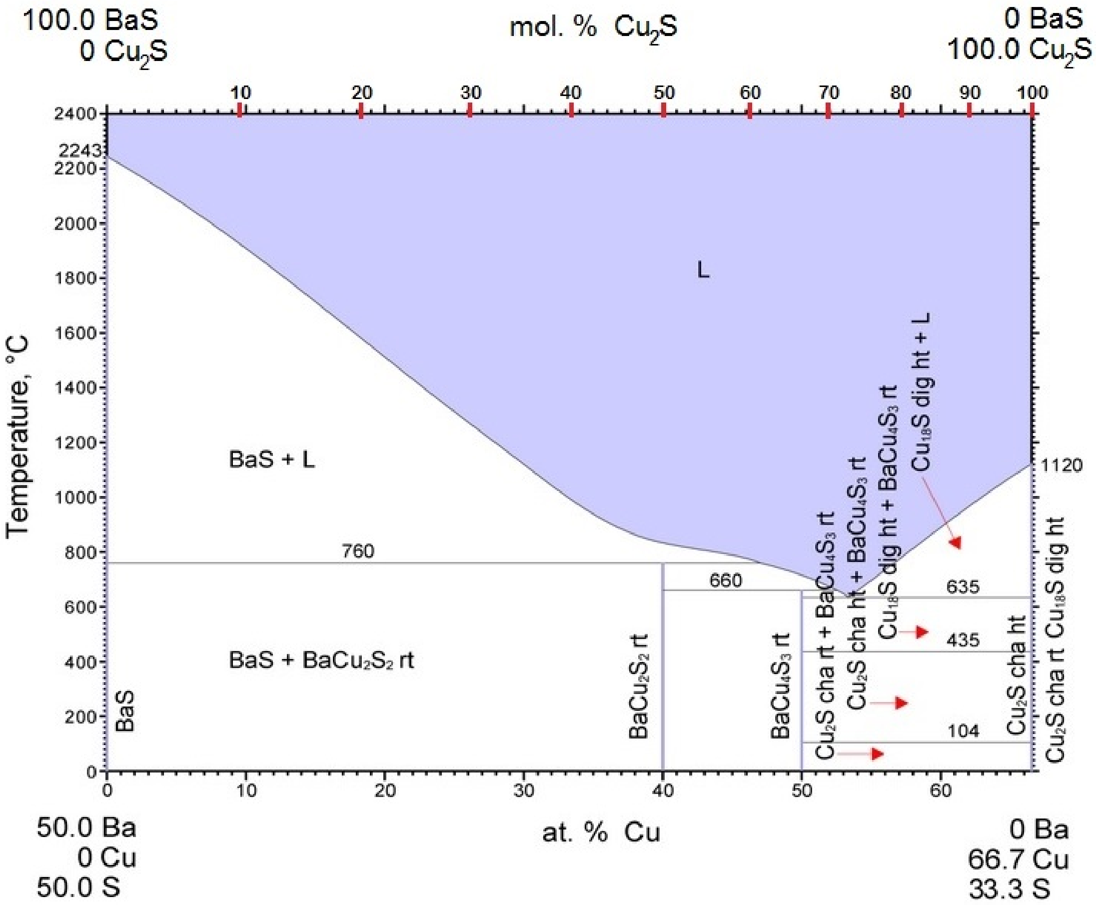

Figure 1-4: Cu_2S-BaS phase diagram [20]

band edge pinning, all potential change occurs in the space charge layer. In Fermi level pinning, potential change occurs across the compact layer [13], causing the barrier height to be constant as a function of applied voltage.

The energy bands for Cu, graphite, Cu_2S, and BaS at room temperature are given in Figure 1-6. Adapting solid-state band theory at higher temperatures will be inaccurate, but it will provide a basis for discussion.

It should be noted that there is also an energy barrier to the transfer of metallic ions from a metal electrode to the electrolyte [13].

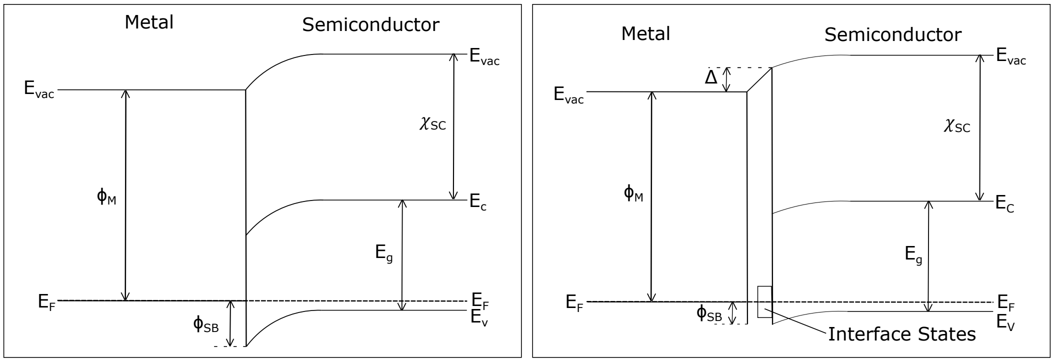

(a)

(b)

Figure 1-5: Band diagrams of a metal-semiconductor (p-type) junction (a) without interface states and (b) with interface states

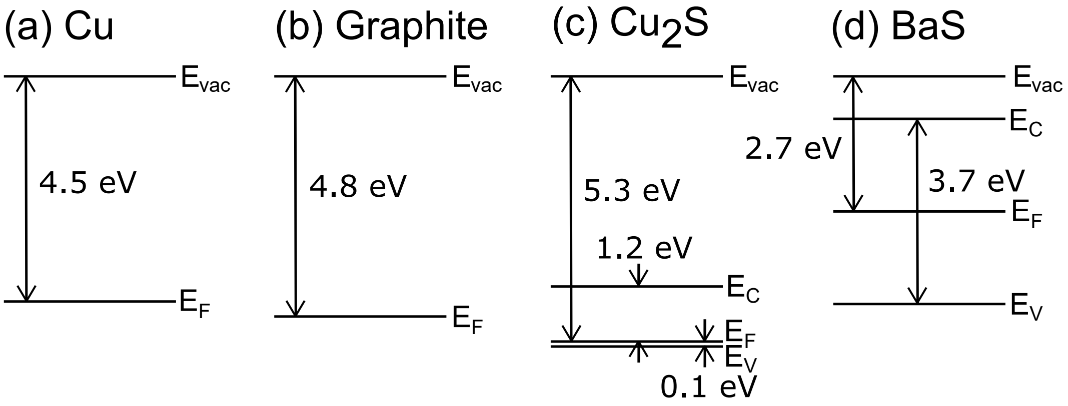

Figure 1-6: Energy levels at room temperature for (a) Cu, (b) Graphite, (c) Cu_2S, and (d) BaS [22, 23, 24, 25, 26]

1.5 Experimental Purpose

This work seeks to determine an appropriate method for determining t_i and t_e in molten metal sulfides. Two methods will be compared: the faradaic efficiency method and the stepped potential chronoamperometry method. These two methods are selected because they measure the flux of two different species: ions and electrons. In addition, applied voltage will be varied in both methods to determine what effect it has on t_i and t_e.

Chapter 2

Experimental Apparatus and Procedures

2.1 Introduction

The material system studied herein is a mixture of copper (I) sulfide (Cu_2S) and barium sulfide (BaS), with varying composition, temperature, and two purities of Cu_2S. Two methods were used in an attempt to measure electronic and ionic transference numbers. The first, a stepped potential chronoamperometry method, aims to measure the steady-state current due to electrons compared with the transient current due to ionic transport. The second, a faradaic efficiency method compares measured mass change at the electrodes to prediction from Faraday's Law.

2.2 Electrolyte Preparation

Copper (I) sulfide (Cu_2S, 99.5% or 99.99% metals basis, hereafter referred to as low or high purity, respectively, Alfa Aesar) and barium sulfide (BaS, 99.7% metals basis, Alfa Aesar) powders were weighed in a polystyrene dish prior to being mixed together with a stainless steel spatula.

The powders were transferred to a graphite crucible ($<$50ppm ash content, turned on lathe or TTK-4 graphite, Ohio Carbon Blank), depicted in Figure 2-1. The graphite crucible was encased in a fused quartz tube purchased from Quartz Plus, Inc., with an inner diameter of 2.2 cm, an outer diameter of 2.5 cm, and a length of 61 cm.

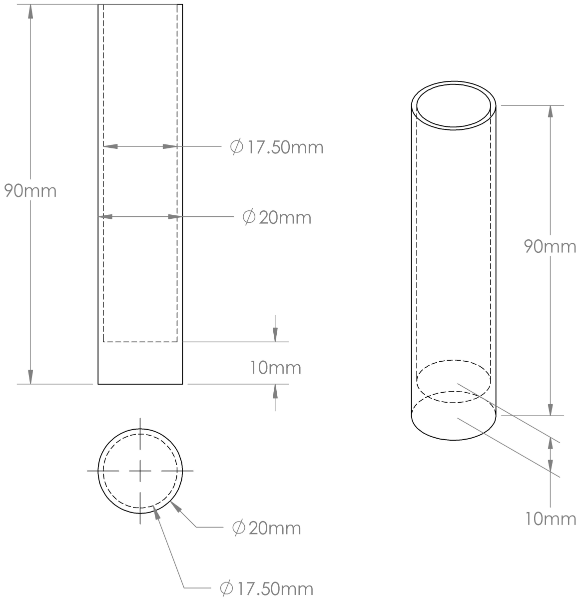

Figure 2-1: Graphite crucible for electrolyte preparation

The quartz tube was maintained under flow of argon (high purity, Airgas) atmosphere in a Lindberg/Blue M Mini-Mite tube furnace. The ensemble was held at room temperature for 30 minutes, then the temperature was increased to 200°C over 1 hour and held at 200°C for 1 hour, with an argon flow rate of 20 mL/min. Argon flow was reduced to less than 1 mL/min and the temperature was increased to 1106°C over 6 hours and held at temperature for 3 hours prior to cooling to room temperature over 2 hours.

The premelted electrolyte was crushed after removal from the furnace and was inspected for copper droplets. Any copper deposits were removed. The premelt was stored in a vial in argon within a storage cabinet purged with nitrogen (4.8 grade, Airgas).

2.3 Stepped Potential Chronoamperometry Measurements

2.3.1 Electrodes

A schematic of the electrode configuration is shown in Figure 2-2. A graphite crucible, as described in the previous section, was used as a counter electrode. A molybdenum wire (3/64 in) lead sheathed in an alumina tube (6.4 mm OD) was threaded into it, and a graphite paste was applied to the junction. The surface area of the electrode exposed to electrolyte was approximately 10 cm^2. Graphite rods (99.9995%, Alfa Aesar) with threaded molybdenum leads sheathed in an alumina tube were used for the working and pseudo-reference electrodes. The graphite rods measured 3.5 mm in diameter and 38.1 mm in length. The graphite rods could be moved together in the z-direction, and movement in the x-y plane was restricted by two graphite spacers (6.4 mm ID and 22 mm OD, with holes to allow gas flow) along the sheathed molybdenum wires. Depending on the immersion depth, the surface area of the graphite rods exposed to the melt varied slightly from experiment to experiment from 0.40 cm^2 to 0.75 cm^2.

2.3.2 Method

Figure 2-3 shows a schematic of the set-up for stepped potential chronoamperometry measurements. The graphite crucible filled with electrolyte and the graphite electrodes were enclosed in a quartz tube capped with two air-cooled Swagelok fittings, connected to an argon (high purity, Airgas) line through push-to-connect fittings. The ensemble was held at room temperature for 30 minutes, then the temperature was increased to 200°C over 30 minutes and held at 200°C for 30 minutes, with an argon flow rate of 20 mL/min. Argon flow was reduced to less than 1 mL/min and the temperature was increased to the operating temperature over 1 hour and held at temperature for 30 minutes before inserting the graphite electrodes. The graphite electrodes were lowered into the melt until electrical contact was made, as deter-

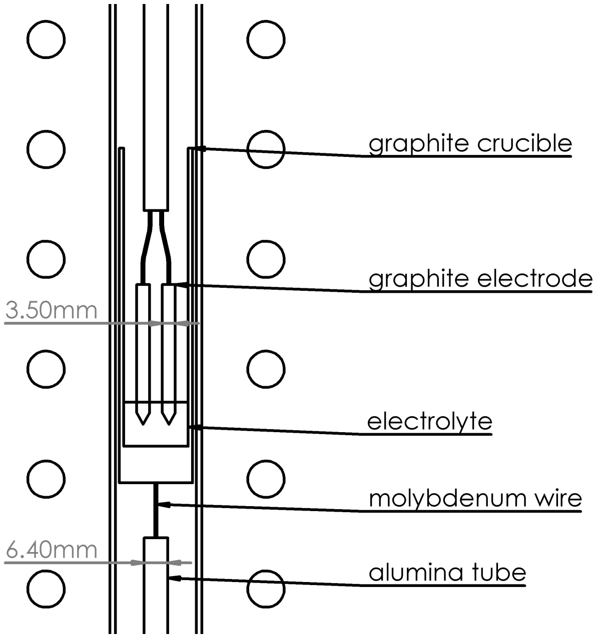

Figure 2-2: Cell geometry and electrode configuration for stepped potential chronoamperometry measurements

mined by applying a small potential (5 mV) across the electrolyte and observing the change in current upon contact. The immersion depth of the electrodes was around 5 mm. After electrochemical measurements at each temperature are completed, the temperature was increased to the next and the system allowed 30 minutes to come to equilibrium. This was repeated for each temperature. After all measurements were completed, the system was allowed to cool down to room temperature over a period of two hours.

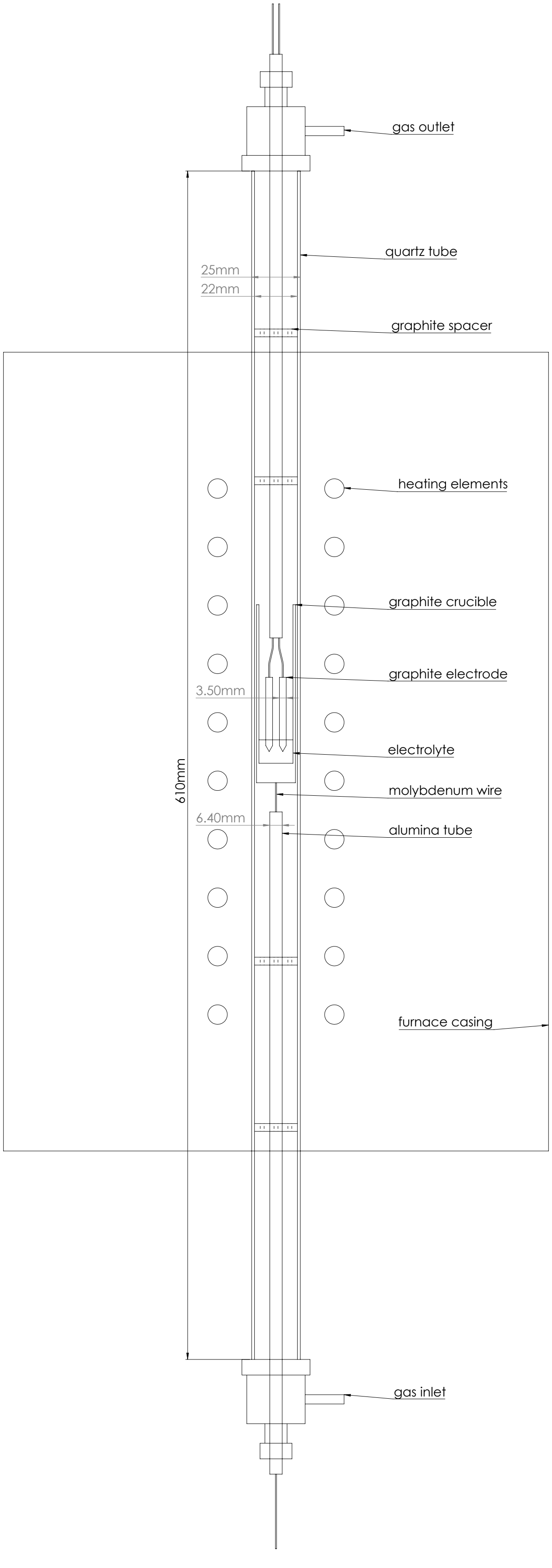

Figure 2-3: Configuration for stepped potential chronoamperometry measurements

2.3.3 Electrochemical Measurements

A Reference 3000 Gamry potentiostat was used to conduct electrochemical measurements. Open circuit potential (OCP), electrochemical impedance spectroscopy (EIS) at OCP, cyclic voltammetry (CV), and stepped potential chronoamperometry measurements were made with the same instrument. The stepped potential chronoamperometry measurements required a high sampling rate. A sampling rate of 20 kHz was obtained using a Data Translation DT9837 analog-to-digital data acquisition system connected to the potentiostat. Measurements were made in the order of OCP, EIS, CV, stepped potential chronoamperometry measurements, EIS again, and OCP again. Stepped potential chronoamperometry measurements were conducted with voltages of ±5, ±10, and ±50 mV. For each stepped potential chronoamperometry measurement, the background current was measured for one minute, the square potential wave was applied for five minutes, and the current was measured for a minute after the applied potential was removed. The system was allowed to re-equilibriate for five minutes before each stepped potential chronoamperometry measurement.

Electronic transference numbers are calculated through Equation 2.1. Figure 2-4 shows I_0, I_{peak}, and $I_{relaxed}$ schematically on an example stepped potential chronoamperometry diagram. I_0 is taken as the average current value prior to the voltage step. I_{peak} is the peak current response to the voltage step, and $I_{relaxed}$ is taken as the average current value over the last minute of the voltage step.

$$t_e = \frac{I_{relaxed} - I_0}{I_{peak} - I_0} \tag{2.1}$$

2.4 Faradaic Efficiency Measurements

2.4.1 Electrodes

A schematic of the electrodes for faradaic efficiency measurements is given in Figure 2-5. The working electrode was composed of a copper rod (99.99%) with a threaded molybdenum wire lead, which was sheathed in an alumina tube (6.4 mm OD). Boron

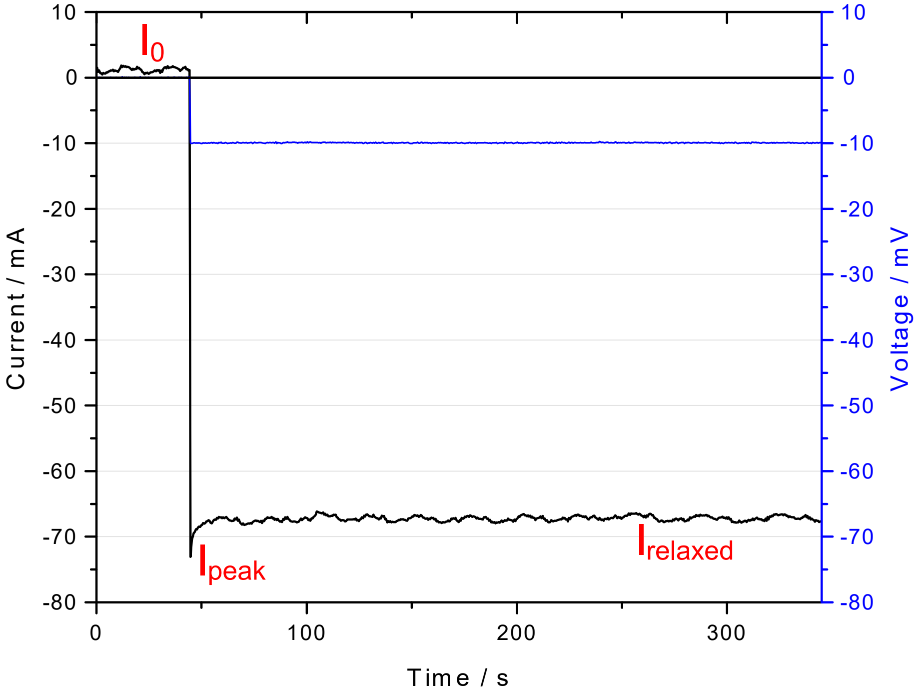

Figure 2-4: Example current response to a potential step showing I_0, I_{peak}, and $I_{relaxed}$

nitride spacers between the alumina sheath and the quartz tube maintained the position of the copper electrode in the center of the quartz tube. The counter electrode used was a copper-tin alloy ($Cu_{0.90}Sn_{0.10}$). The counter electrodes were liquid at the operating temperature, and an electrical connection was made between the bottom of the graphite crucible and the liquid cathode. The inner walls of the graphite crucible were sheathed with an alumina tube (17.5 mm OD, 12.7 mm ID). The graphite crucible was connected to a threaded molybdenum wire lead, sheathed in an alumina tube (6.4 mm OD) and stabilized with boron nitride spacers. The copper-tin alloys were prepared from copper shot (99.999%, Alfa Aesar) and either tin shot (Mallinckrodt) or tin turnings (99.98%, Alfa Aesar). The copper and tin were melted together in an arc melter (MAM 1, Edmund Bühler GmbH) with a tungsten electrode. The chamber of the arc melter was subjected to three vacuum and argon (high purity, Airgas) purge cycles prior to use. The hearth of the arc melter was water cooled. A zirconium pellet was melted first in order to act as an oxygen getter. The copper and tin were then melted, flipped, and melted again, striving towards compositional homogeneity.

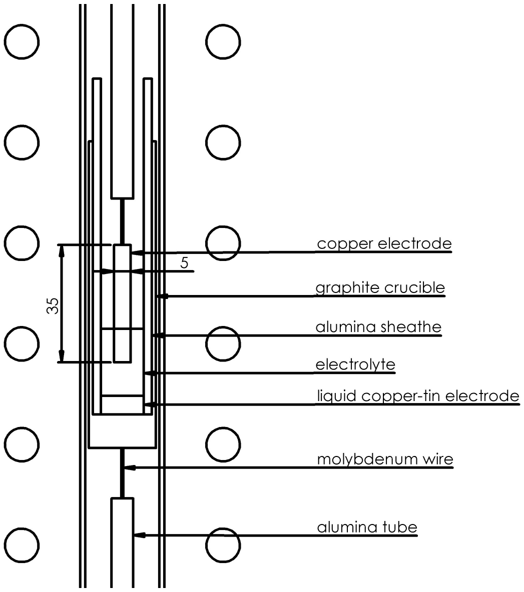

Figure 2-5: Cell geometry and electrode configuration for faradaic efficiency measurements

2.4.2 Method

Figure 2-6 shows a schematic of the set-up for faradaic efficiency measurements. The $Cu_{0.90}Sn_{0.10}$ electrode was placed at the bottom of the graphite crucible and electrolyte was added above the $Cu_{0.90}Sn_{0.10}$ electrode. The copper electrode was suspended and centered above the electrolyte. The ensemble was enclosed in a 74 cm long quartz tube closed with air-cooled Swagelok fittings connected to an argon line with push-to-connect fittings. The ensemble was held at room temperature for 30 minutes, then the temperature was increased to 200°C over 30 minutes and held at 200°C for 30 minutes, with an argon flow rate of 20 mL/min. Argon flow was reduced to less than 1 mL/min and the temperature was increased to 950°C over 1 hour and held at temperature for 30 minutes before inserting the copper electrode. The copper electrode was lowered into the melt until electrical contact was made, as determined by OCP measurements. The effect of having the copper electrode in contact with the melt without applied potential is minimal, as explained in Appendix A. The copper electrode was then lowered into the melt at a consistent melt depth of 5 mm. A potential of either 0.2184 V over 30 minutes or 0.0200 V over 2.5 hours was applied. The copper electrode was then raised out of the melt while the potential was still being applied. The furnace was then reset, the insulation removed, and the quartz tube (and therefore also the crucible) was raised by 12 cm to the point where the bottom of the crucible was positioned above the opening at the top of the tube furnace. Fans were then pointed at the region of the quartz tube containing the crucible.

2.4.3 Electrochemical Measurements

A Reference 3000 Gamry potentiostat was used to conduct electrochemical measurements. Open circuit potential (OCP), electrochemical impedance spectroscopy (EIS) at OCP, and galvanostatic measurements were conducted with the same instrument.

2.4.4 Analysis

Samples were stored within a storage cabinet with a nitrogen (4.8 grade) atmosphere prior to being ground and polished. Each crucible was sectioned in two vertically with a low speed diamond saw (Model 650, South Bay Technology, Inc.). The samples were then ground with 180, 320, 600, and 1200 grit silicon carbide papers with a kerosene lubricant. The samples were cleaned with cotton balls soaked in acetone and dried with air between grits. The samples were polished with 5μm, 1μm, and 0.25μm diamond paste (MetaDi, Bühler) with a kerosene lubricant. A $K_2Cr_2O_7$ etchant (2g of $K_2Cr_2O_7$ in 5mL of saturated NaCl solution, 8mL of H_2SO_4, and 100mL of H_2O) was applied by rubbing an etchant-soaked sterile cotton ball on the Cu-Sn samples for 10 seconds. The etchant was then washed off in cold water, cleaned with soapy water, and dried. Polished and etched samples were stored in a desiccator. The samples were then imaged with optical microscopy (Olympus BX51). A JEOL JSM-6610LV scanning electron microscope (SEM) equipped with a Sirius SD detector for energy dispersive spectroscopy (EDS) was used for elemental analysis. The etched samples were polished again with diamond paste prior to being analyzed with a JEOL JXA-8200 Superprobe through wavelength dispersive spectroscopy (WDS).

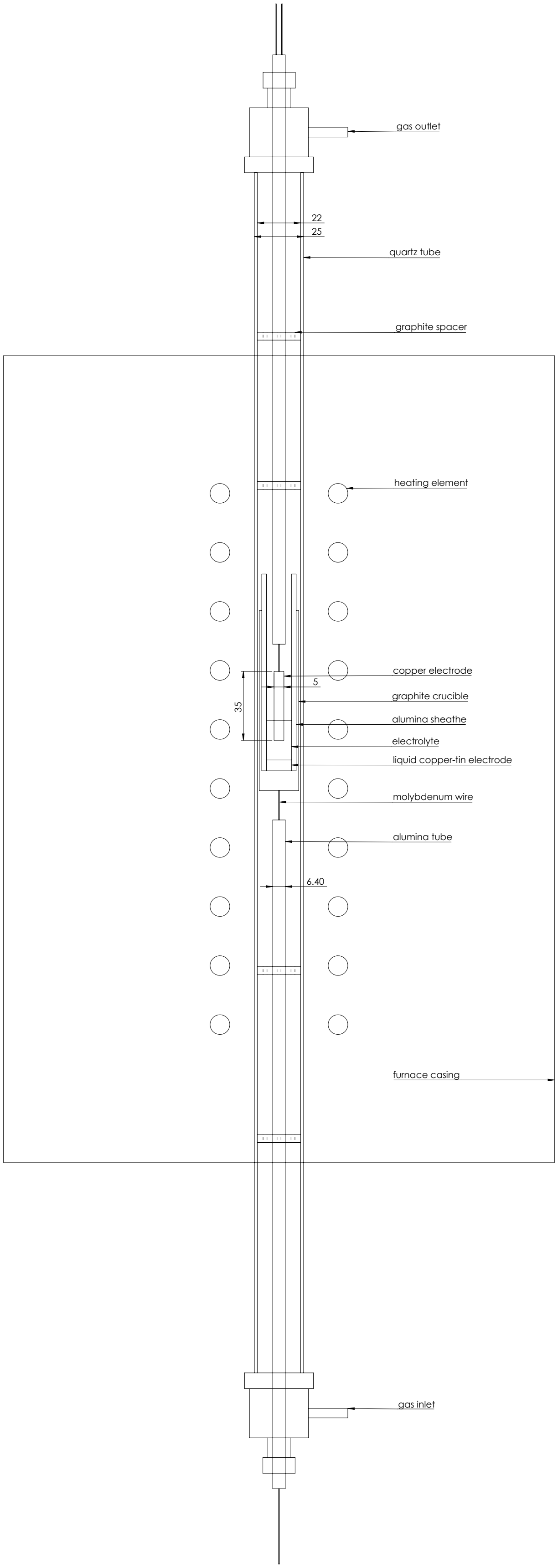

Figure 2-6: Configuration for faradaic efficiency measurements

The solidified copper-tin electrode has a dendritic microstructure. The phase diagram for the copper-tin binary is presented in Figure 2-7. Compositions of the α-phase dendrites were determined through both EDS and WDS, taking measurements in a grid-like pattern and through line scans, as shown in Figure 2-8. The composition of the copper-rich α phase in a $Cu_{0.90}Sn_{0.10}$ sample from a blank experiment in which potential was not applied is determined by SEM/EDS to range from 88.31 at% Cu to 96.24 at% Cu, which, when compared to the copper-tin phase diagram in Figure 2-7, is not physical, as the minimum α composition should be 91 at%. When measured by WDS, the copper content ranged from 91.05 at% to 95.96 at%, which matches the phase diagram well. As a result, WDS is used for all compositional estimates.

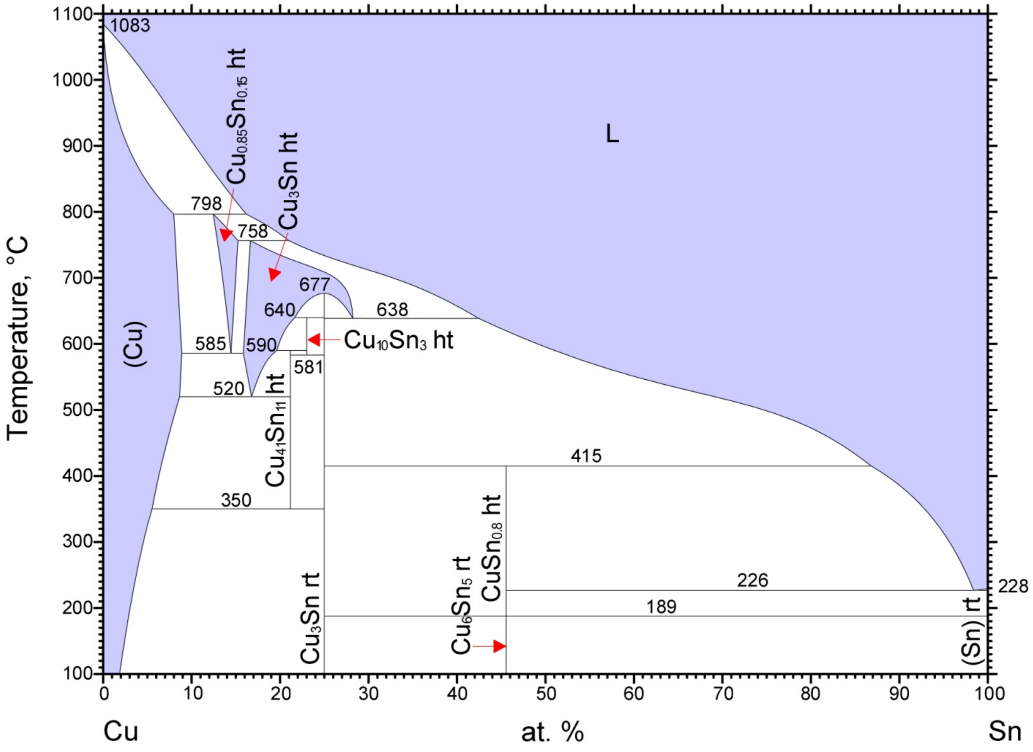

Diagram No. 904768

Figure 2-7: Copper-tin phase diagram [27]

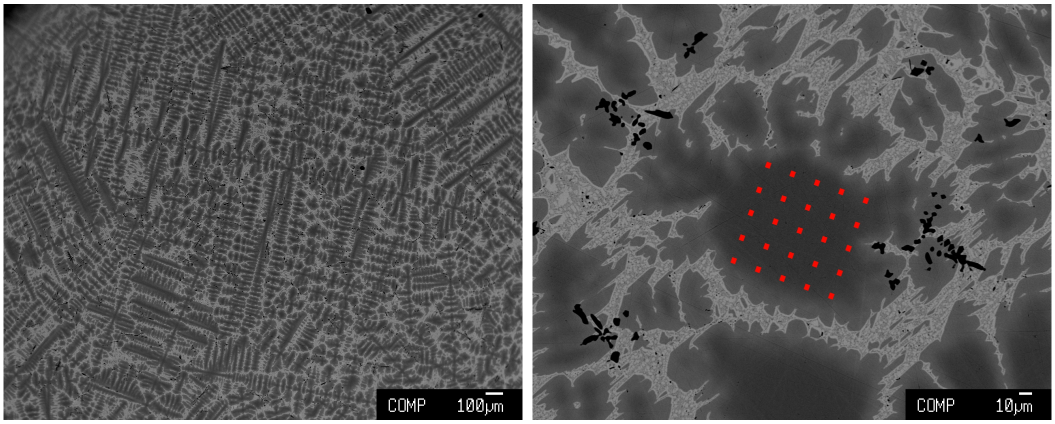

(a) Copper-tin electrode micrograph (b) Grid pattern

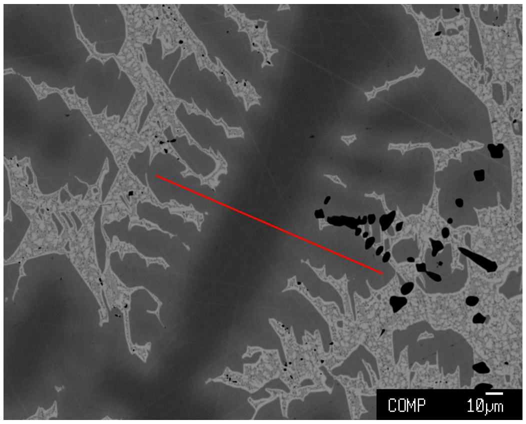

(c) Line scan

Figure 2-8: (a) Low-zoom micrograph of copper-tin electrode (the black regions are Cu_2S, the darker grey regions are Cu-rich, and the lighter grey regions are a mixture of the Cu-rich phase and Cu_3Sn) and higher-zoom micrographs showing the (b) grid and (c) line scan sampling patterns used for composition measurements using EDS and WDS

2.4.5 Method of Faradaic Efficiency Estimation

Faradaic efficiency is estimated through a comparison of the anodic mass loss and cathodic mass gain to the mass loss predicted through Faraday's law. Appendix B compares the accuracy of multiple methods investigated to compute the change of mass at the anode and cathode. The most accurate of these methdos are listed in the subsections below.

Direct Measurement of Mass Change of the Anode and Cathode

Anodic mass loss is estimated through the mass change of the copper electrode. The cathode was easily separated from the electrolyte after solidification, and its change in mass is measured.

External Analysis of the Cathode

The cathode was sent to Luvak Laboratories, Inc. (Boylston, MA), an external analytical laboratory, for direct current plasma emission spectroscopy (DCPES) using ASTM standard E1097. The change in copper mass was then calculated from the measured composition.

Estimation of the Cathode Composition

Micrographs of the cathode were analyzed with an image analysis software, Image J, to generate a histogram, such as the one shown in Figure 2-9. The area fraction corresponding to each phase composition is calculated from the pixel counts at each pixel intensity.

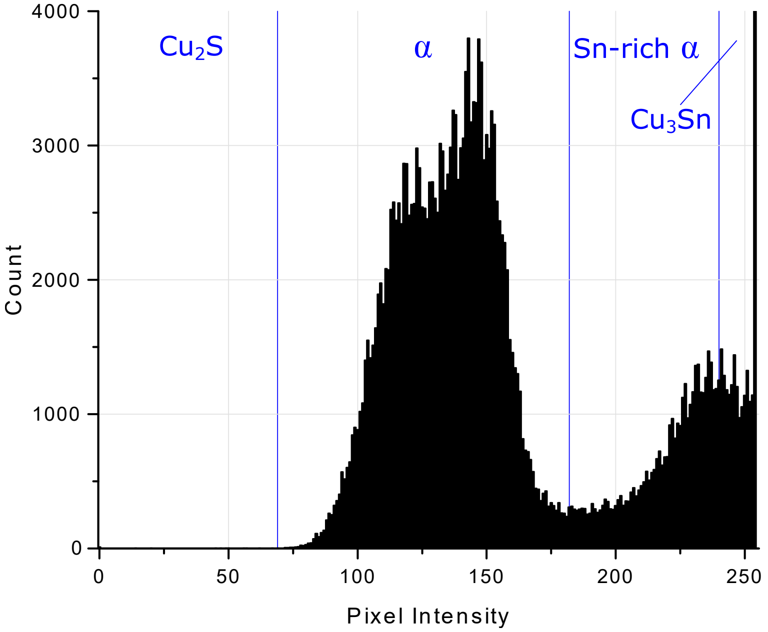

Figure 2-9: Pixel intensity histogram from the copper-tin cathode from a blank experiment without application of voltage at 950°C

The α phase corresponds with the large peaks at low intensity, where the range in pixel intensity corresponds with the range of the α phase composition. The smaller peak at high intensity corresponds with a mixture of the most tin-rich α and Cu_3Sn. The darker half of the peak is attributed to the tin-rich α, and the lighter half of the peak is attributed to the Cu_3Sn. There are small amounts of Cu_2S at low intensity that were filtered out for the purpose of area fraction estimation. There were small amounts of the $(Cu_2S)_{0.73}(BaS)_{0.27}$ electrolyte in some of the cathodes. These electrolyte phases had to be manually identified and filtered out, as their intensities overlapped with that of the α phase.

The most copper-rich composition measured by WDS from the α dendrites and the least copper-rich α composition from the phase diagram are taken as the end points for the α composition range, and the rest of the α composition range is linearly interpolated between those points. The half of the peak attributed to the tin-rich α is assigned a single composition: the least copper-rich α composition from the phase diagram. The half of the peak attributed to the Cu_3Sn is assigned a single composition: the composition of the line compound from the phase diagram.

Chapter 3

Results

3.1 Introduction

Results from the two experimental methods are presented. In the first method, electronic transference numbers are directly estimated from stepped potential chronoamperometry. In the same experiments, the solution resistance between the electrodes are estimated by EIS measurements. In the second method, ionic transference numbers are estimated from faradaic efficiency measurements.

First, the transference numbers from these two methods are compared for one composition of the electrolyte, namely $(Cu_2S)_{0.73}(BaS)_{0.27}$. t_e estimated with stepped potential chronoamperometry are presented as a function of temperature and applied voltage for two purities of Cu_2S, and the t_i estimated with faradaic efficiency are presented as a function of applied potential at a single temperature. The change in solution resistance with temperature from EIS measurements is presented after the transference numbers.

Second, t_e estimated by stepped potential chronoamperometry for a range of Cu_2S-BaS electrolytic compositions are presented as a function of temperature and applied voltage for two purities of Cu_2S. For each of these compositions, the change in solution resistance with temperature from EIS measurements is also presented.

3.2 Electronic Transference Number of $(Cu_2S)_{0.73}(BaS)_{0.27}$

In this section, the only electrolyte composition studied is $(Cu_2S)_{0.73}(BaS)_{0.27}$, which is 71.8 wt% Cu_2S and 28.2 wt% BaS. This is the eutectic composition, which melts at 635°C, as can be seen on the phase diagram given in Figure 1-4. For stepped potential chronoamperometry measurements, the temperature range investigated is from 650°C to 1050 °C (a superheat of 15°C to 415°C). All faradaic efficiency experiments were performed at 950°C (a superheat of 315°C).

3.2.1 Stepped Potential Chronoamperometry

Stepped chronoamperometry experiments are completed with graphite rods as the working and reference electrodes and a graphite crucible as the counter electrode, as described in Section 2.3.1. In principle, this method estimates t_e from current measurements.

Figure 3-1 shows the result from a stepped potential chronoamperometry experiment at 1050°C and an applied voltage step of -10mV. The mean current before the voltage step is 1.25 mA, the trough current is -73.08 mA occurring 16 ms after the voltage step, and the mean current after relaxation is -67.17 mA. t_e is calculated to be 0.920.

The corresponding t_e are reported in Table 3.1 for varying temperatures and two purities of Cu_2S. t_e decreases with temperature for high purity Cu_2S, but that trend reverses for low purity Cu_2S, as t_e increases with temperature. The estimated magnitude of t_e are greater when a high purity Cu_2S is used than when a low purity Cu_2S is used.

t_e changes with applied voltage, as shown in Figure 3-2a and Figure 3-2b for electrolytes prepared with pure and impure Cu_2S, respectively. t_e increases with increasingly positive applied voltage. Both positive and negative voltages were applied in the high purity Cu_2S, and the rate of change of t_e with applied voltage is greater for positive applied voltage than for negative applied voltage.

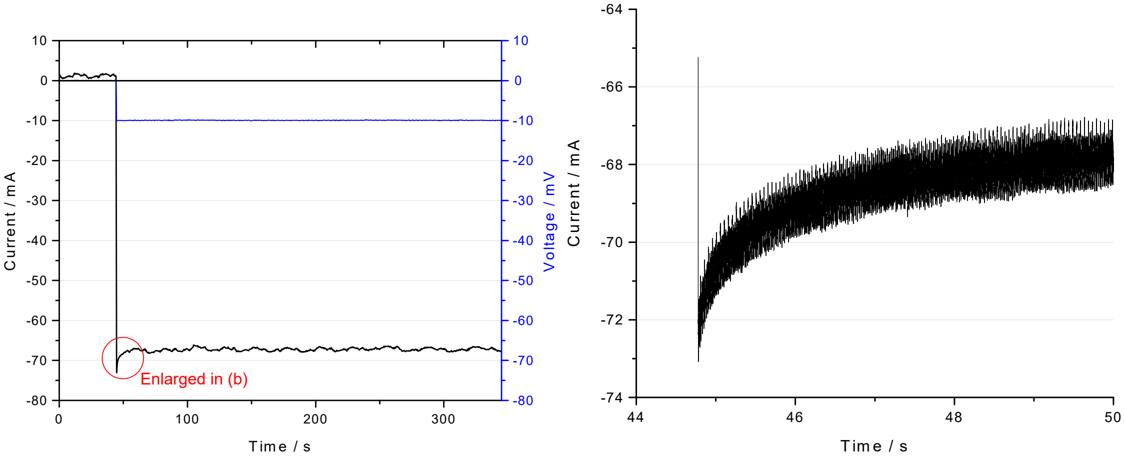

(a) (b)

Figure 3-1: (a) Current response to an applied voltage of -10 mV at 1050°C with a $(Cu_2S)_{0.73}(BaS)_{0.27}$ electrolyte with high purity Cu_2S. (b) Enlarged peak current response

Table 3.1: Electronic transference numbers as a function of temperature and Cu_2S purity estimated with stepped potential chronoamperometry using a -10 mV applied voltage with a $(Cu_2S)_{0.73}(BaS)_{0.27}$ electrolyte

Temperature (°C)	Low Purity (99.5%) Cu_2S	High Purity (99.99%) Cu_2S
650	0.652	n/a
750	n/a	0.951
850	0.728	0.937
1050	0.855	0.920

3.2.2 Faradaic Efficiency

Faradaic efficiency experiments are completed with a solid copper rod as the anode and a liquid copper-tin pool ($Cu_{0.90}Sn_{0.10}$)) as the cathode, as described in Section 2.4.1. This method estimates ionic transference numbers. Example current traces from experiments with two different applied voltages, 20 mV for 2.5 hours and 218.4 mV for 30 minutes, are presented in Figure 3-3. The cathode gains copper content after application of the voltage.

In the faradaic efficiency experiments, applied voltage has the same effect on t_i (and thus on t_e) as reported for stepped potential chronoamperometry measurements, as shown in Figure 3-2. The copper-tin cathode (initially $Cu_{0.90}Sn_{0.10}$) gains copper after the experiment. In a "blank" experiment without applied voltage where a copper

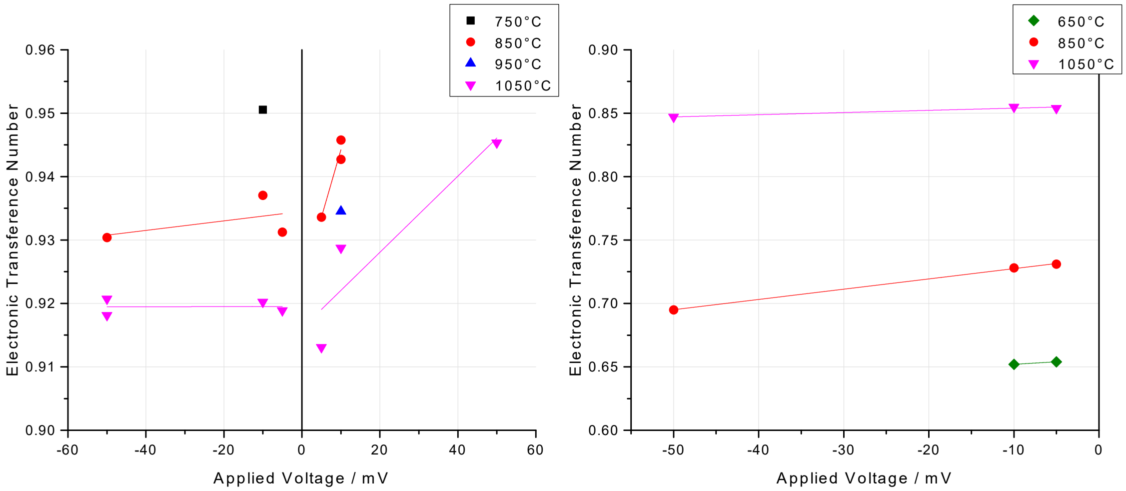

(a) (b)

Figure 3-2: Electronic transference numbers as a function of voltage and temperature estimated with stepped potential chronoamperometry with a $(Cu_2S)_{0.73}(BaS)_{0.27}$ electrolyte prepared with (a) high purity Cu_2S and (b) low purity Cu_2S

rod is immersed for 30 minutes, the final composition of the copper-tin is determined to be $Cu_{0.898}Sn_{0.102}$, as described in Appendix B. The copper content of the copper-tin pool is greater after experiments in which voltage is applied. The final cathodic compositions are reported in Table 3.2 for experiments with an electrolyte with low purity Cu_2S.

Table 3.2: Cathode composition estimates after faradaic efficiency experiments with a $(Cu_2S)_{0.73}(BaS)_{0.27}$ electrolyte with low purity Cu_2S

Applied Voltage (mV)		Charge Passed (C)	External Analysis Composition (at% Cu)	Continuous Image Analysis (Max found to min PD) Composition (at% Cu)
20	1	1232	n/a	90.99
	2	1024	91.25	91.22
218.4	1	2310	91.62	91.65
	2	1480	91.24	91.03
	3	1492	91.25	90.83

While the copper electrode loses mass during experiment, it also gains an external layer of sulfide and copper, as shown in Figure 3-4 for a "blank" run in which no potential was applied, and the copper rod was submerged for 30 minutes. The copper in the external layer has a tin content of 0.76 at%, higher than the tin content in

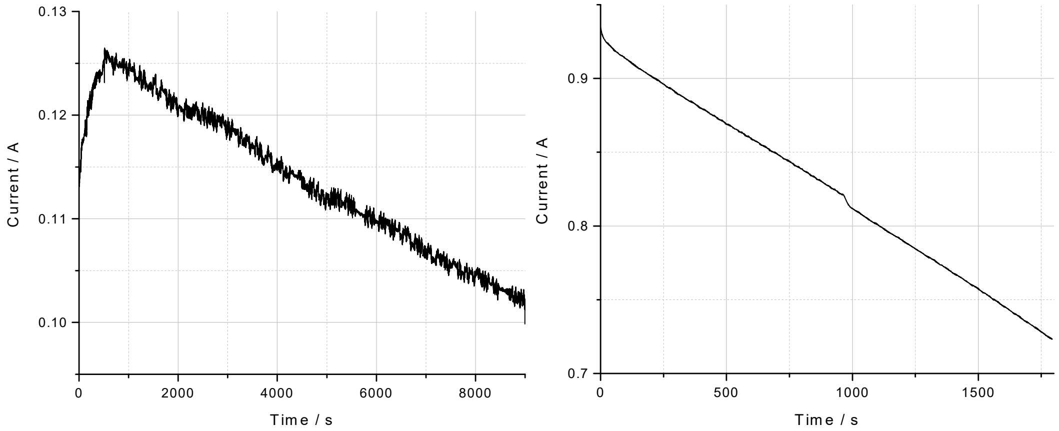

(a) 20 mV applied for 2.5 hours (b) 218.4 mV applied for 30 minutes

Figure 3-3: Current traces from faradaic efficiency experiments at 950°C with a $(Cu_2S)_{0.73}(BaS)_{0.27}$ electrolyte prepared with low purity Cu_2S

the bulk of the copper rod, which has a tin content of 0.03 at%. The detection limit of WDS for tin is 41.1 ppm. Interestingly, in both locations, the copper also has a barium content of at least 0.10 at% (the detection limit of WDS for Ba is 30.1 ppm), which may have been transferred from the sulfide during polishing. Additionally, the size of the external layer solidified on the outside of the copper rod increases with immersion time in the melt. The copper electrode gained a larger external layer for experiments with an applied potential of 20 mV over 2.5 hours than it did for experiments with an applied voltage of 218.4 mV over 30 minutes, as can be seen in Figures 3-5a and 3-5b, respectively.

t_i estimated through cathodic composition change decreases with increasing applied voltage, as reported in Table 3.3. The anodic mass loss results do not show the same trend, but this is expected, acknowledging the larger solid masses on the outside of the copper electrode that accompany longer immersion times.

t_e corresponding to the t_i estimated by the faradaic efficiency method are smaller than the t_e estimated by the stepped potential chronoamperometry, and both sets of t_e increase with applied potential.

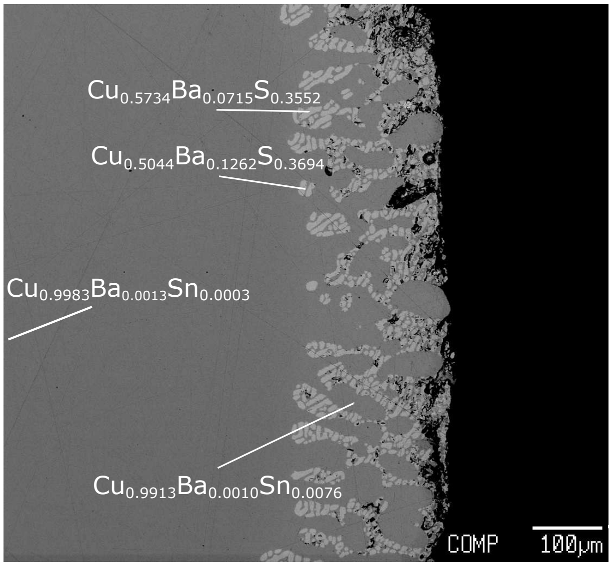

Figure 3-4: Surface of the copper electrode after immersion into and removal from the melt

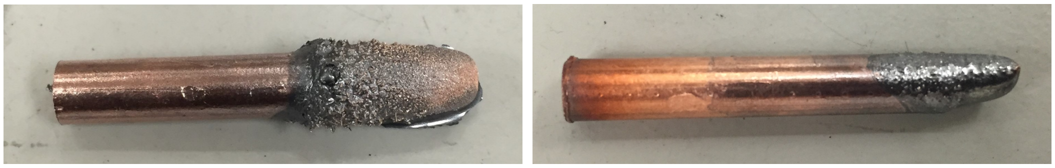

(a) 20 mV applied

(b) 218.4 mV applied

Figure 3-5: Copper anodes after faradaic efficiency experiments showing the accumulation layer along the previously submerged length and the change from the initial cylindrical shape

3.2.3 Conductivity

Solution resistance of the electrolyte is determined through EIS measurements taken prior to stepped chronoamperometry experiments and are completed with graphite rods as the working and reference electrodes and a graphite crucible as the counter electrode, as described in Section 2.3.1.

The solution resistance of the electrolyte decreases with temperature when high purity Cu_2S is used, as presented in Table 3.4. This suggests that the electrolyte acts as a semiconductor.

Table 3.3: Ionic transference numbers from faradaic efficiency experiments with a $(Cu_2S)_{0.73}(BaS)_{0.27}$ electrolyte with low purity Cu_2S. *: The anode showed accumulation of electrolyte after experiments

Applied Voltage (mV)		Charge Passed (C)	Ionic Transference Number			
			Anode*	Cathode		
			Mass Loss	Mass Gain	External Analysis	Continuous Image Analysis
20	1	1232	0.307	0.815	n/a	0.625
	2	1024	0.306	0.944	0.974	0.948
218.4	1	2310	0.647	0.587	0.585	0.597
	2	1480	0.673	0.729	0.669	0.546
	3	1492	0.673	0.723	0.668	0.424

Table 3.4: Solution resistance as a function of temperature from EIS measurements with a $(Cu_2S)_{0.73}(BaS)_{0.27}$ electrolyte prepared with high purity Cu_2S

Temperature (°C)	Resistance (Ω)	Conductance (S)
750	0.194	5.15
850	0.145	6.91
950	0.139	7.20
1050	0.135	7.41

3.3 Effect of BaS Content in Electrolyte

In this section, electrolytes are studied with varying BaS content via stepped potential chronoamperometry. The investigated experimental temperatures range from 650°C to 1156°C. All measurements were conducted above the liquidus, but the extent of superheat depends upon the specific composition and temperature.

3.3.1 Electronic Transference Numbers Estimated by Stepped Potential Chronoamperometry

t_e as a function of composition and temperature is presented in Figure 3-6 for electrolytes with high purity Cu_2S. As the BaS content in electrolytes with high purity Cu_2S is increased, t_e decreases. t_e decreases with temperature across the entire electrolyte composition range in this study.

t_e as a function of composition and temperature is presented in Figure 3-7 for electrolytes with low purity Cu_2S. When the electrolyte is prepared with a low purity

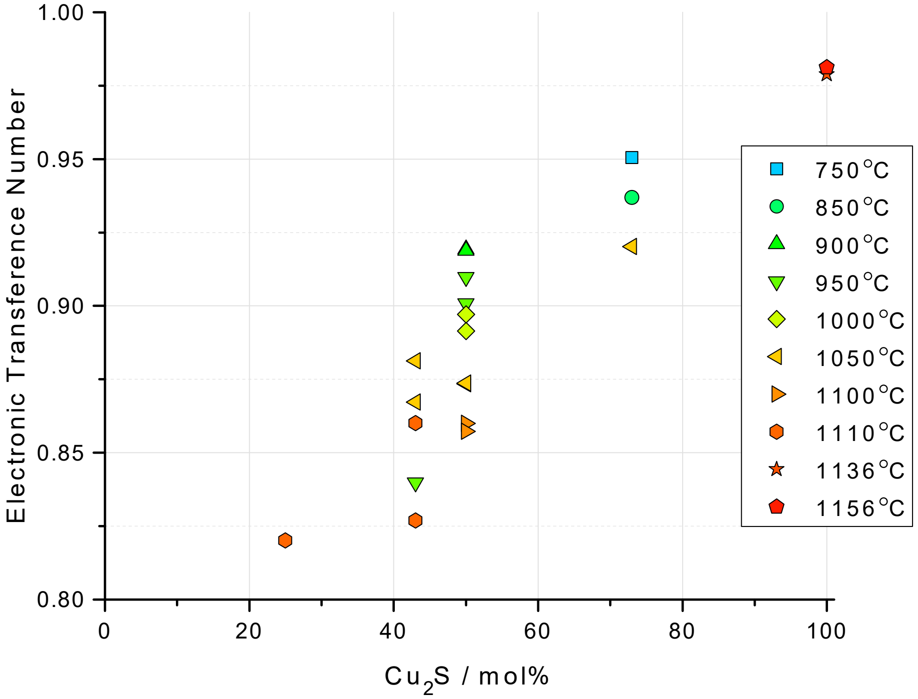

Figure 3-6: Electronic transference numbers as a function of electrolyte composition and temperature estimated with stepped potential chronoamperometry using a -10 mV applied voltage with electrolytes prepared using high purity Cu_2S

Cu_2S, the change in t_e with composition is not evident. The variation of t_e with temperature is inconsistent across the investigated composition range.

When comparing Figures 3-6 and 3-7, it can be seen that the magnitude of t_e estimated when the low purity Cu_2S is used is lower than when the high purity Cu_2S is used.

3.3.2 Conductivity

The solution resistance change with temperature varies across the composition range. The rate of change is given in Table 3.5. The rate of change decreases with increasing Cu_2S content in the electrolyte. For one electrolytic composition, $(Cu_2S)_{0.73}(BaS)_{0.27}$ with high purity Cu_2S, the solution resistance decreases with temperature.

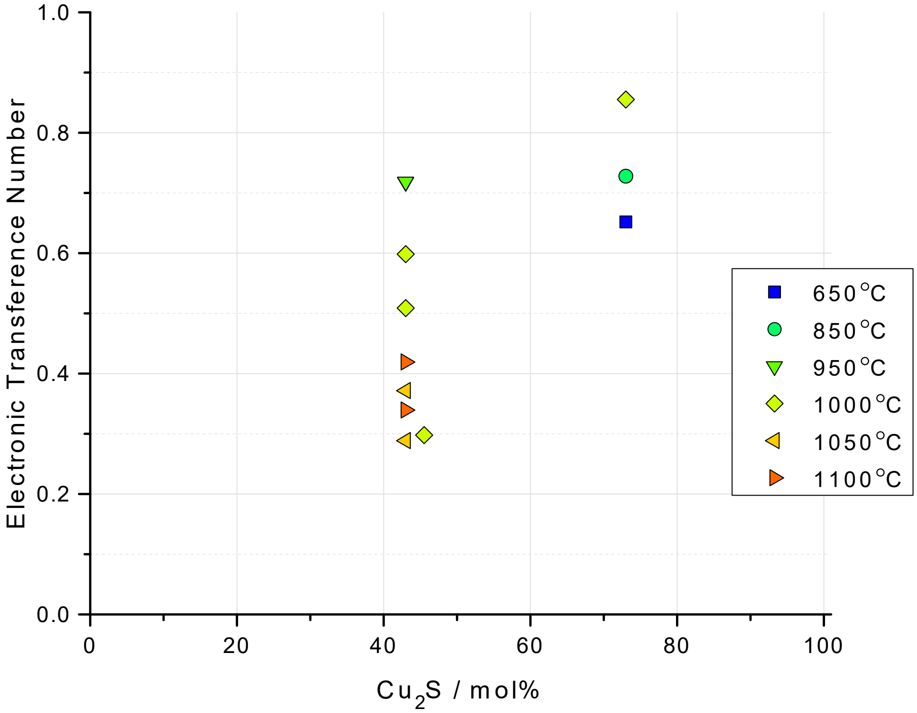

Figure 3-7: Electronic transference numbers as a function of electrolyte composition and temperature estimated with stepped potential chronoamperometry using a -10 mV applied voltage with electrolytes prepared using low purity Cu_2S

Table 3.5: Rate of change of solution resistance with temperature as a function of electrolyte composition

Cu_2S Purity	Mol% Cu_2S	Resistance/°C (Ohm/°C)	Conductance/°C (S/°C)
99.5% (Low purity)	43	0.178	-0.00487
99.99% (High purity)	25	7.130	-0.0742
	43	0.125	-0.00520
	50	0.054	-0.00199
	73	-0.183	0.00705

Chapter 4

Discussion

The electronic transference numbers estimated through stepped potential chronoamperometry are significantly higher than those estimated through faradaic efficiency. We shall attempt to explain this discrepancy through three approaches: (1) the role of the work function of the electrode material, (2) the role of the additional alloying driving force in faradaic efficiency experiments and (3) the role of tin impurities in the electrolyte. We will discuss experimental evidence for each proposed explanation and propose future experiments to investigate their validity.

We shall also discuss the effect of the BaS content in the electrolyte with respect to the electrolyte electronic behavior and its relation with the hypothesized structure of the melt. Additional related experiments are proposed to substantiate this discussion.

4.1 Electrode Work Function

First, we shall investigate the role that the electrode choice might play in the electronic transference number measurements.

4.1.1 Comparison of Faradaic Efficiency and Stepped Potential Chronoamperometry Electrodes

We shall use schematics of the electronic band structure of the heterojunctions between the electrodes and molten electrolyte to examine the potential effects of the work functions of the electrodes and of the applied voltage. It should be noted that we lack a detailed understanding of the band structure of molten Cu_2S-BaS melts. The following discussion will make the following simplifying assumptions: (1) the electronic energy levels of the $(Cu_2S)_{0.73}(BaS)_{0.27}$ melt will be treated as those of solid Cu_2S at room temperature, with p-type semi-conductor behavior (as suggested by its positive Seebeck coefficient [4]), (2) the work functions of graphite, Cu, and $Cu_{0.90}Sn_{0.10}$ are the same as those measured in vacuum at 298K, and (3) there are no interface states (as shown in Figure 1-5a) between the electrodes and the electrolyte.

Band diagrams of the electrode-electrolyte interfaces for the stepped potential chronoamperometry and faradaic efficiency electrode configurations without applied voltage are presented in Figure 4-1. The difference between the work function of Cu and the electronegativity of the electrolyte is greater than that between the work function of graphite and the electronegativity of the electrolyte. This leads to a larger Schottky barrier when Cu is used as an electrode, as seen in Figure 4-1b as compared to Figure 4-1a.

We can calculate how the change in Schottky barrier height can be expected to change the electronic transference number, given the electronic transference number corresponding to a known Schottky barrier height. We will use 0.12, the electronic transference number estimated via the faradaic efficiency method at 950°C with an applied voltage of 20 mV, to estimate what the electronic transference number from stepped potential chronoamperometry measurements with a graphite electrode would be under the same conditions.

We begin by assuming that the steady state ionic current increases linearly with applied voltage but does not change with the height of the Schottky barrier [13]. The electronic current will increase according to Equation 4.1, where $I_{e,s}$ is the electronic

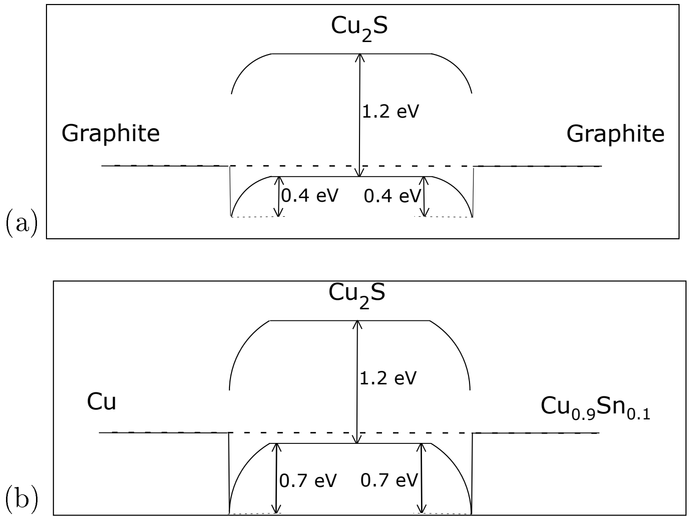

Figure 4-1: Band diagrams of the electrode-electrolyte heterojunctions present in (a) stepped potential chronoamperometry experiments and (b) faradaic efficiency experiments without externally applied voltage

reverse saturation current, V is the applied voltage, and k_B is the Boltzmann constant.

$$I_e = I_{e,s}(e^{\frac{V}{k_B T}} - 1) \tag{4.1}$$

The electronic reverse saturation current, $I_{e,s}$, contains the dependence upon the Schottky barrier height, Φ_{SB}, as described in Equation 4.2.

$$I_{e,s} \propto e^{-\frac{\Phi_{SB}}{k_B T}} \tag{4.2}$$

We can then write t_e in Equation 4.3 as a function of the Schottky barrier height, neglecting the impact of the applied voltage, in terms of ionic and electronic currents, I_i and I_e, respectively.

$$t_e(\Phi_{SB}) = \frac{I_e(\Phi_{SB})}{I_e(\Phi_{SB}) + I_i} \tag{4.3}$$

With knowledge of t_e with a specified Schottky barrier ($\Phi_{SB,1}$) and applied voltage (V), we can calculate an expected t_e at another voltage barrier, $\Phi_{SB,2}$, at the same applied voltage without explicit knowledge of the magnitude of the ionic current, as described in Equations 4.4 and 4.5. $\Phi_{SB,1}$ will correspond to the case where a Cu electrode is used, and $\Phi_{SB,2}$ will correspond to the case where a graphite electrode is used.

$$t_e(\Phi_{SB,2}) = \frac{I_e(\Phi_{SB,2})}{I_e(\Phi_{SB,2}) + I_i} \tag{4.4}$$

$$t_e(\Phi_{SB,2}) = \frac{\frac{I_e(\Phi_{SB,2})}{I_e(\Phi_{SB,1})}}{\frac{I_e(\Phi_{SB,2})}{I_e(\Phi_{SB,1})} + \frac{I_i}{I_e(\Phi_{SB,1})}} \tag{4.5}$$

First, we use Equation 4.6 to calculate the relative magnitudes of electronic current as a function of the height of the voltage barrier.

$$\frac{I_e(\Phi_{SB,2})}{I_e(\Phi_{SB,1})} = e^{\frac{\Phi_{SB,1} - \Phi_{SB,2}}{k_B T}} \tag{4.6}$$

The heights of the Schottky barriers at the interfaces between graphite and Cu_2S and between Cu and Cu_2S are 0.4 eV and 0.7 eV, respectively. We consider the case where 20 mV is applied at 950°C. Plugging these values into Equation 4.6, we obtain Equation 4.7.

$$\frac{I_e(0.4)}{I_e(0.7)} = e^{\frac{0.7-0.4}{8.617 \cdot 10^{-5} \cdot 1223}} = 17.23 \tag{4.7}$$

Second, we plug in 0.12 as $t_e(\Phi_{SB,1})$ into Equation 4.8, to calculate the relative magnitude of ionic current as compared to the electronic current at the reference voltage barrier, as shown in Equation 4.9.

$$\frac{I_i}{I_e(\Phi_{SB,1})} = \frac{1 - t_e(\Phi_{SB,1})}{t_e(\Phi_{SB,1})} \tag{4.8}$$

$$\frac{I_i}{I_e(0.7)} = \frac{1 - 0.12}{0.12} = 7.33 \tag{4.9}$$

Next, using Equation 4.10 we compute the t_e that would be expected when a graphite electrode is used given the difference in barrier height as compared to the case where a Cu electrode is used.

$$t_e(0.4) = \frac{17.23}{17.23 + 7.33} = 0.70 \tag{4.10}$$

This result strongly suggests that the Schottky barrier causes a large difference between t_e estimated using the two experimental methods used in this work. Using the t_e of 0.12 estimated using a Cu electrode (as in faradaic efficiency experiments) allows us to calculate a corresponding t_e of 0.70 under the same conditions when a graphite electrode is used (as is used in stepped potential chronoamperometry experiments). The values of t_e estimated experimentally with stepped potential chronoamperometry at 850°C and 1050°C at an applied voltage of 10mV are 0.73 and 0.86, which indicate a relative increase on the same order of magnitude as predicted via Equation 4.10. The calculated t_e underestimates the t_e obtained via stepped potential chronoamperometry, but this underestimation could be due to the assumptions made about the values of the work functions of the electrode materials and the energy levels of the electrolyte.

4.1.2 Influence of Applied Voltage in Faradaic Efficiency Experiments

In similar calculations, the influence of applied voltage on t_e can be investigated in faradaic efficiency experiments. Equation 4.1 presents the dependence of the electronic current on applied voltage. When keeping Φ_{SB} constant by using the same electrode material, t_e can be written in terms of applied voltage, V, as shown in Equation 4.11.

$$t_e(V) = \frac{I_e(V)}{I_e(V) + I_i(V)} \tag{4.11}$$

With knowledge of t_e at a specified applied voltage V_1, we can calculate an expected t_e at another applied voltage V_2 without explicit knowledge of the magnitude of the ionic current, as described in Equations 4.12 and 4.13.

$$t_e(V_2) = \frac{I_e(V_2)}{I_e(V_2) + I_i(V_2)} \tag{4.12}$$

$$t_e(V_2) = \frac{\frac{I_e(V_2)}{I_e(V_1)}}{\frac{I_e(V_2)}{I_e(V_1)} + \frac{I_i(V_2)}{I_e(V_1)}} \tag{4.13}$$

First, we use Equation 4.14 to calculate the relative magnitudes of electronic current as a function of applied voltage.

$$\frac{I_e(V_2)}{I_e(V_1)} = \frac{e^{\frac{V_2}{k_B T}} - 1}{e^{\frac{V_1}{k_B T}} - 1} \tag{4.14}$$

Second, we calculate the relative magnitude of ionic current as compared to the electronic current at the reference voltage barrier V_1, as shown in Equation 4.15.

$$\frac{I_i(V_2)}{I_e(V_1)} = \frac{V_2}{V_1} \cdot \frac{1 - t_e(V_1)}{t_e(V_1)} \tag{4.15}$$

An increase in t_e as a function of applied voltage is observed in faradaic efficiency experiments, as t_e increases from 0.12 when a voltage of 20 mV is applied to 0.34 when a voltage of 218.4 mV is applied. By using $V_1 = 20$ mV and $t_e(V_1) = 0.12$ as a reference point, we can plug in results from Equations 4.14 and 4.15 into Equation 4.13, obtaining t_e as a function of applied voltage, as shown in Figure 4-2. The t_e predicted at 218.4 mV is 0.29, slightly under the t_e of 0.34 obtained from faradaic efficiency measurements. While this data matches Equation 4.13 fairly well, more data points are needed to confirm the trend.

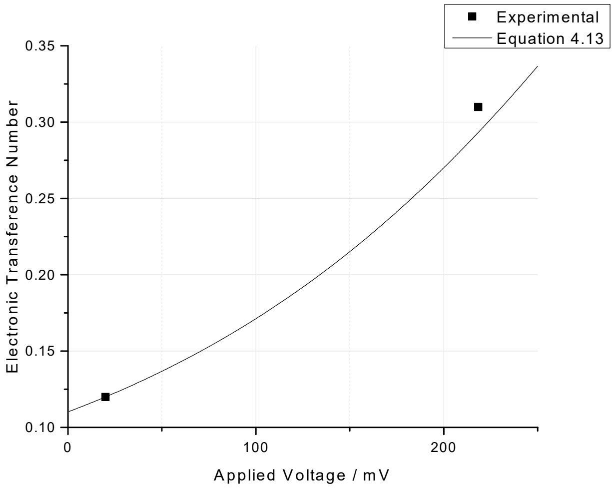

Figure 4-2: Comparison of experimental and calculated electronic transference numbers as a function of applied voltage from faradaic efficiency experiments at 950°C with a $(Cu_2S)_{0.73}(BaS)_{0.27}$ electrolyte prepared with low purity Cu_2S

4.1.3 Influence of Applied Voltage in Stepped Potential Chronoamperometry Experiments

Figure 4-3 shows the expected effect of applied voltage on the band diagrams when graphite electrodes are used. As holes will travel from the positively charged electrode to the negatively charged one, the only change in barrier height that they will "see" is the shrinking of the barrier at the negatively charged electrode.

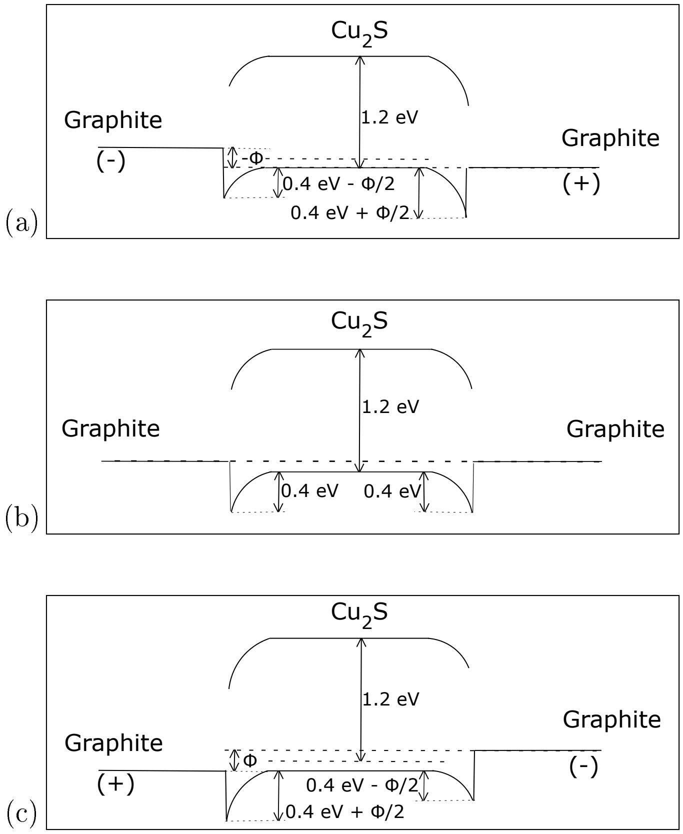

Figure 4-3: Band diagrams of graphite electrode-electrolyte heterojunctions with (a) negative applied voltage, (b) no applied voltage, and (c) positive applied voltage

The change in t_e with applied potential from stepped potential chronoamperometry experiments, presented in Figure 3-2, shows an increase in t_e with increasing magnitude of applied voltage only when the applied voltage is positive. Using the analysis described in Section 4.1.2, we can estimate a value for t_e at various applied voltages by plugging t_e at $V_1 = 5$ mV into Equation 4.13, as shown in Figure 4-4. The estimation underpredicts the relative increase in t_e with applied voltage. When the applied voltage is negative, t_e slightly decreases as the magnitude of the applied voltage is increased. This does not agree with the expected behavior from our simple model.

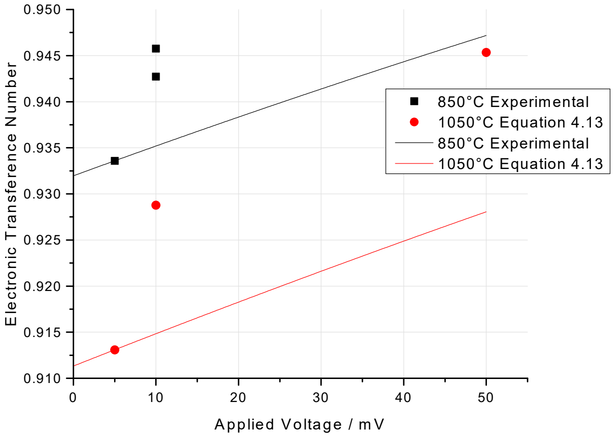

Figure 4-4: Comparison of experimental and calculated electronic transference numbers as a function of applied voltage from stepped potential chronoamperometry experiments at 850°C and 1050°C with a $(Cu_2S)_{0.73}(BaS)_{0.27}$ electrolyte prepared with high purity Cu_2S.

In order to address the disagreement between this simple model and the results from stepped potential chronoamperometry, we should reexamine our simplifying assumptions. The change in t_e with applied voltage is asymmetrical. This should not be the case if the two graphite electrodes are identical, but they are not. In the present study, the surface areas of the working electrode and counter electrodes are approximately 0.6 cm^2 and 10 cm^2, respectively. The current density is then more than 10 times as large at the working electrode, as presented in Figure 4-5. Our third simplifying assumption that there are no interface states at the interface between the electrode and the electrolyte may be wrong if the current density is too high. Figure 4-6 shows the band diagrams of the graphite-electrolyte heterojunctions assuming that the Fermi level at one junction (at the working electrode) is pinned due to surface states. The barrier height at that electrode will not be changed as the applied voltage is changed.

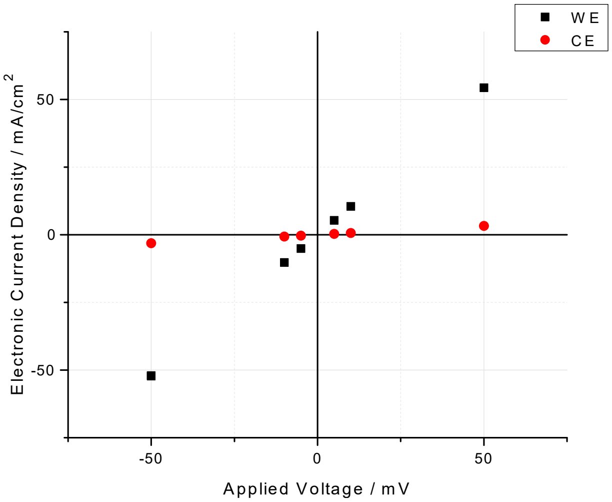

Figure 4-5: Electronic current density at the working electrode (WE) and at the counter electrode (CE) as a function of applied voltage from stepped potential chronoamperometry experiments at 1050°C with a $(Cu_2S)_{0.73}(BaS)_{0.27}$ electrolyte prepared with high purity Cu_2S

Challenging the assumption that there are no interfacial states shines a better light on the data. When the working electrode is positively charged, t_e still increases with voltage, but when the working electrode is negatively charged, the barrier to electronic conduction is unchanged with magnitude of applied voltage. The data from Figure 3-2 shows that at negative applied potential, t_e slightly decreases as applied voltage becomes more negative.

4.1.4 Proposed Future Work

To verify the hypothesized role of the work function of the electrodes, new experiments should be conducted with electrodes of various work functions. If an electrode that had a work function closer to the Fermi level of the electrolyte is used for stepped potential chronoamperometry, we would expect to see t_e increase. Likewise, if an electrode with a work function further from the electrolyte Fermi energy is used, we would expect to the t_e decrease. Care should be taken that the electrodes are chemically stable in the electrolyte. Alternatively, the electron affinity and/or band gap of the electrolyte can be changed, but without a better description of the electronic structure of the liquid electrolye, the Schottky barrier height cannot be modulated

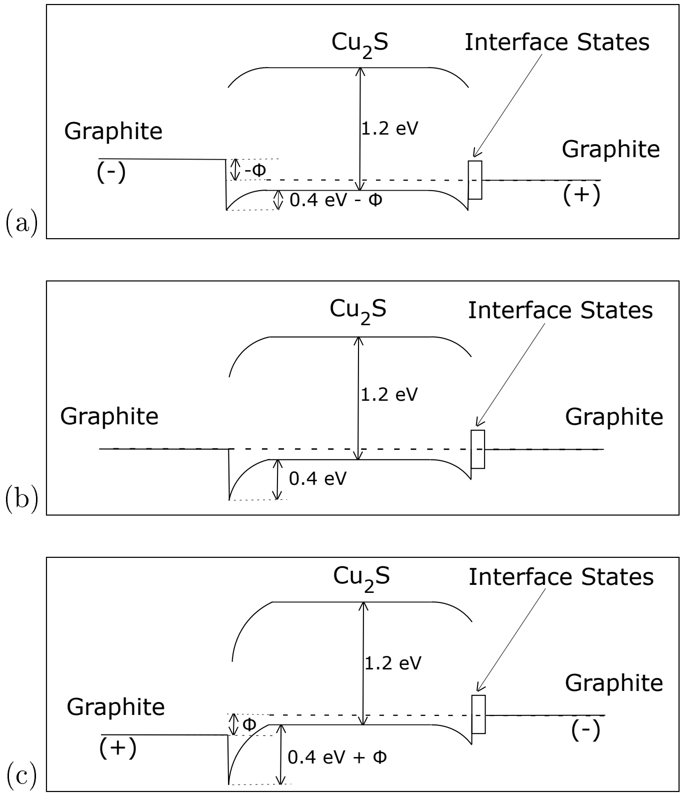

Figure 4-6: Band diagrams of graphite electrode-electrolyte heterojunctions with (a) negative applied voltage, (b) no applied voltage, and (c) positive applied voltage assuming that the Fermi level at one electrode is pinned due to interfacial states

with certainty. Time resolved photoelectron spectroscopy [28] provides a description of the density of states of a liquid as a function of the energy relative to the Fermi level. This could be used to get a better description of the band gap (or pseudogap), but to date this technique is not available for molten sulfides.

To verify the dependence of the I_e and t_e on applied voltage, faradaic efficiency experiments should be conducted over a larger range of applied voltages, as two points is not enough to draw a strong conclusion.

In order to verify the role of current density at the electrodes in pinning the Fermi energy of the electrolyte, a new stepped potential chronoamperometry experiment should be conducted with electrodes of equal geometry. If our hypothesis is true, then t_e should be symmetrical across positive and negative applied voltages.

4.2 Alloying Driving Force

Second, we will consider another aspect of the consequences of electrode material choice. There is an additional driving force for Cu ions to alloy into the Cu-Sn cathode in faradaic effiency experiments that is not present in stepped potential chronoamperometry experiments. The influence of the additional driving force on the magnitude of t_e will be determined. In addition, the decrease in current with time observed during experiments will be analyzed considering the change in driving force as Cu alloys into the Cu-Sn electrode and considering geometrical changes during the experiment.

4.2.1 Influence of Alloying Driving Force on Electronic Transference Numbers

In faradaic efficiency experiments, copper will be oxidized at the Cu anode, according to Equation 4.16, and copper ions in the electrolyte will be reduced at the Cu-Sn cathode, according to Equation 4.17.

$$Cu \rightarrow Cu^{+} + e^{-} \tag{4.16}$$

$$Cu^{+} + e^{-} \rightarrow Cu \text{ (in } Cu_{1-x}Sn_{x}) \tag{4.17}$$

The activity of solid Cu in the liquid Cu-Sn cathode at 950°C is determined using Factsage and is presented in Figure 4-7. The driving force for alloying can be calculated through the "galvanic" cell voltage E_{galv} according to Equation 4.18, where R is the gas constant, z is the charge number (1, in this case), F is Faraday's constant, $a_{Cu \text{ (in } Cu_{1-x}Sn_{x})}$ is the activity of Cu in $\text{Cu}_{1-x}\text{Sn}_{x}$, and a_{Cu} is the activity of pure Cu. The "galvanic" cell voltage at 950°C is presented in Figure 4-8.

$$E_{galv} = \frac{RT}{zF} ln \left(\frac{a_{Cu \text{ (in } Cu_{1-x}Sn_{x})}}{a_{Cu}} \right) \tag{4.18}$$

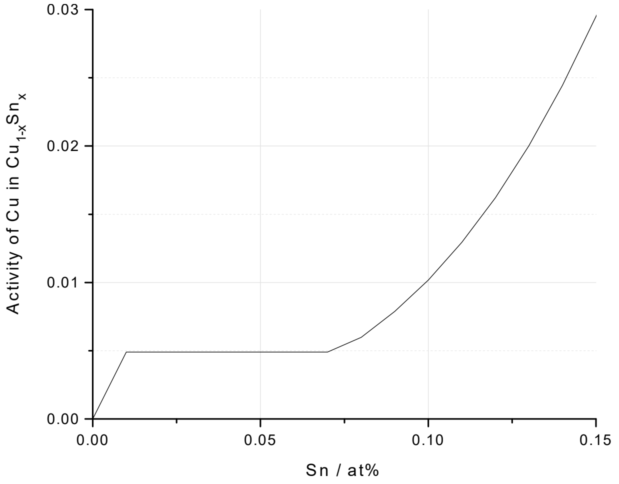

Figure 4-7: Activity of Cu in $Cu_{1-x}Sn_x$ at 950°C

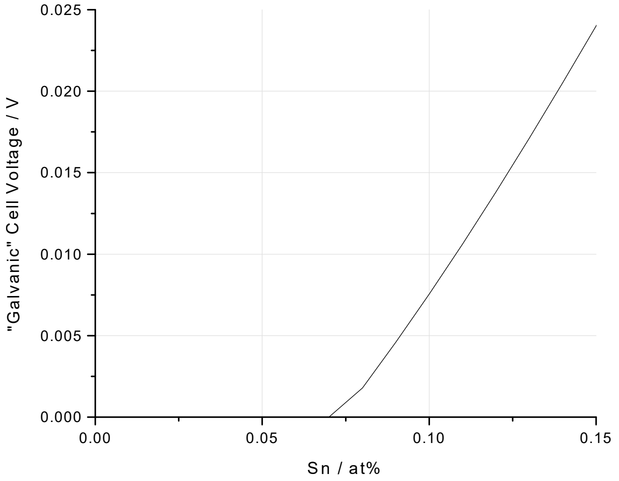

Figure 4-8: "Galvanic" cell voltage between solid copper and liquid $Cu_{1-x}Sn_x$ at 950°C

At the beginning of the experiment, the composition of the cathode is $Cu_{0.90}Sn_{0.10}$, which corresponds to a "galvanic" cell voltage of 7.55 mV. According to Figure 4-2, if this "galvanic" driving force of 7.55 mV was removed, t_e determined by the faradaic efficiency method would be approximately 3% smaller. Therefore, the additional driving force due to alloying is not expected to contribute to the difference between t_e determined by the two methods. This is supported by evidence from a "blank" experiment where no potential was applied, so the only driving force present was the driving force to alloy. There was no detectable transfer of Cu from the solid Cu electrode to the liquid $Cu_{0.90}Sn_{0.10}$ electrode, as discussed in Appendix B.

4.2.2 Investigating the Decrease in Current with Time

The driving force for Cu to alloy into the Cu-Sn electrode may have another effect. The current traces obtained from faradaic efficiency experiments show a decrease in current with time, which could be due to either the change in driving force as Cu alloys into the Cu-Sn, the change in distance between the anode and the cathode during the experiment, or a diffusion limitation. We shall investigate the change in driving force first.

The effective voltage across the electrolyte is the sum of the "galvanic" cell voltage from the compositional differences between the electrodes and the applied voltage between the electrodes. At the beginning of the experiment, the composition of the cathode is $Cu_{0.90}Sn_{0.10}$, which corresponds to a "galvanic" cell voltage of 7.55 mV. At the end of both experiments, the composition of the cathodes are $Cu_{0.9125}Sn_{0.0875}$ when 20 mV is applied and $Cu_{0.9124}Sn_{0.0876}$ when 218.4 mV is applied. Those two compositions correspond to "galvanic" cell voltages of 3.93 mV and 3.90 mV, respectively. The composition is assumed to change as a function of the charge passed through the cell, from which E_{galv} is calculated as a function of time. The resistance of the electrolyte is calculated with Equation 4.19.

$$R = \frac{V_{applied} + E_{galv}(t)}{I} \tag{4.19}$$

The length of the Cu anode is measured before and after experiments. The length of the Cu electrode shortens by 0.66 mm and 1.73 mm when 20 mV and 218.4 mV are applied, respectively. The initial distance between electrodes is 5 mm in both cases. The resistance of the electrolyte will increase as a function of the distance between the electrodes, as shown in Equation 4.20, where κ is the conductivity of the electrolyte, l is the distance between the electrodes, and A is the cross-sectional area of the cell [21].

$$R = \frac{1}{\kappa} \cdot \frac{l}{A} \tag{4.20}$$

The experimentally measured current, the current calculated based on the change of alloying content at the cathode, and the current calculated based on the change of distance between the electrodes are plotted in Figure 4-9.

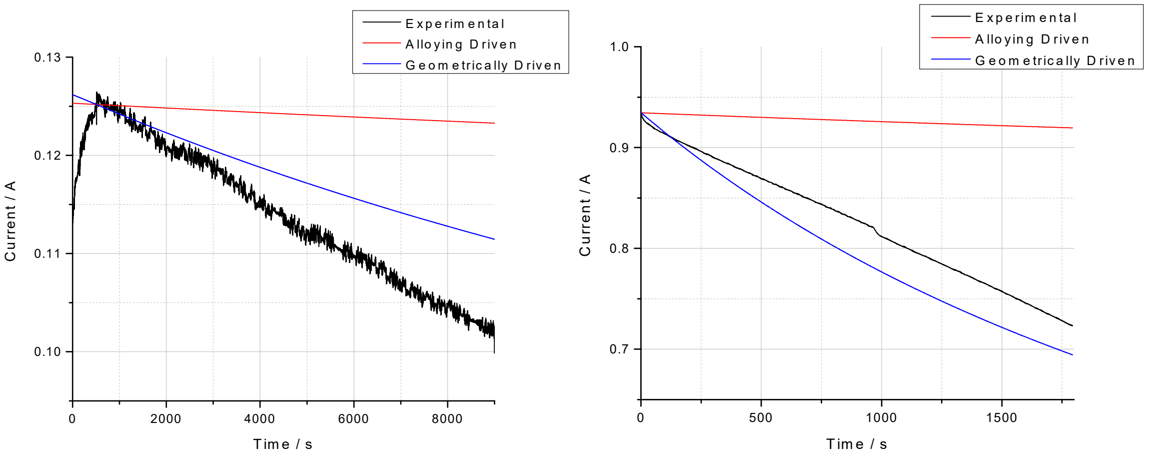

(a) 20 mV applied for 2.5 hours (b) 218.4 mV applied for 30 minutes

Figure 4-9: Comparison of experimental current, current predicted due to change in Cu-Sn composition, and current predicted due to change in electrode spacing as a function of time during faradaic efficiency experiments at 950°C with a $(Cu_2S)_{0.73}(BaS)_{0.27}$ electrolyte prepared with low purity Cu_2S

While both experimental factors are accompanied by a decrease in current, these results indicate that the decrease in current is mostly due to the increase in distance between the anode and the cathode as copper is transported from the Cu anode to the Cu-Sn cathode rather than due to the change in composition at the Cu-Sn cathode.

Diffusion may also limit the current. The diffusion constant of Cu in Cu_2Se is $2.6 \cdot 10^{-5}$ at 1120°C [4], just above the melting point of Cu_2Se. Using this diffusion constant as an approximation of that in Cu_2S, we can calculate the width of the diffusion layer, L, to be 0.22 cm and 0.48 cm when potential is applied for 30 minutes and 2.5 hours, respectively, using Equation 4.21, where D_{Cu} is the diffusion constant [29].

$$L = \sqrt{D_{Cu}t} \tag{4.21}$$

If the current is diffusion limited, it should follow the Cottrell equation in Equation 4.22, where n is the number of electrons, A is the area of the cathode, and c^0_{Cu} is the initial concentration of Cu ions in the electrolyte [29].

$$I = \frac{nFAc_{Cu}^{0}\sqrt{D_{Cu}}}{\sqrt{\pi t}} \tag{4.22}$$

The current in Figure 4-9 does not show a $t^{-1/2}$ dependence. As a result, diffusion limitation is not taken to be the cause of the decrease in current as a function of time.

4.2.3 Proposed Future Work

The driving force for Cu to alloy into Cu-Sn could be made insignificant by using a cathode with less than 7 at% Sn.

To determine whether the change in distance between electrodes causes the decrease in current with time, one should use an anode that has a larger diameter. The shortening of the anode could then be compensated by an increase in height at the cathode if the densities of the electrodes are taken into account.

4.3 Tin Impurities in the Electrolyte

Third, we must consider the possibility that it is not the electrodes, but rather the electrolyte that causes the differences between the experiments. To this end, we investigate the presence of small amounts of tin impurities (<0.5 at%) in the electrolyte and their possible effect on t_e. These impurities may come from two sources: tin impurities in the Cu_2S used in making the electrolyte and tin from the $Cu_{0.90}Sn_{0.10}$ electrode used in faradaic efficiency experiments.

The purity of Cu_2S used has an effect on t_e, as can be seen by comparing results from stepped potential chronoamperometry experiments in Figures 3-6 and 3-7, where the Cu_2S used is 99.99% pure and 99.5% pure, respectively. The tin impurities are accompanied by a decrease in t_e of about 30% on average.

t_e measured by faradaic efficiency experiments are significantly lower than those measured by stepped potential chronoamperometry experiments. Studies on the stability of Cu-Sn alloys in the presence of the $(Cu_2S)_{0.73}(BaS)_{0.27}$ electrolyte, as detailed in Appendix A, show small concentrations of Sn in the electrolyte (<2 at%) and small

(<3 μm) inclusions of Cu_3Sn, as shown in Figure A-1. The Cu_3Sn inclusions become larger and more numerous with increasing Sn content in the Cu-Sn alloy, suggesting that some tin is gained in the electrolyte from the Cu-Sn alloy. The liquid $Cu_{0.90}Sn_{0.10}$ electrode is therefore considered as a possible source of tin in the electrolyte.

The nature of the tin inclusions in the melt is not clear; there may be molten metallic Sn or Cu-Sn alloys or molten tin-containing sulfides. The phase diagram of Sn-S is presented in Figure 4-10. There is a miscibility gap between the Sn-rich liquid and a more sulfide-rich liquid. A miscibility gap is also observed in an isothermal section of the Cu-Sn-S ternary phase diagram at 1200°C, which is presented in Figure 4-11. The Cu_3Sn inclusions found may have solidified from a liquid of a composition close to Cu_3Sn on the S-poor side of the miscibility gap. While a phase diagram is not given explicitly for the quaternary system of Cu-Ba-Sn-S, it is reasonable to assume that a miscibility gap is still present, and both a molten Cu-Sn alloy and a molten sulfide containing Sn could be present in the electrolyte.

SnS has a p-type character above its melting point, as indicated by its positive Seebeck coefficient [32], and a very similar electronic structure to Cu_2S at room temperature with an electron affinity that is smaller by 0.2 eV [33], which would theoretically shrink the Schottky barrier. If it has any effect, the addition of SnS would be expected to therefore increase the electronic conductivity of the electrolyte, not decrease it.

The addition of metallic Cu-Sn alloys may have a more dramatic effect. The addition of an extra metallic phase may disrupt the short-range order presumed to be present in the electrolyte and provide a new path for electrons through percolation through the metal network.

4.3.1 Proposed Future Work

In order to verify that addition of tin to the electrolyte decreases t_e, experiments should be conducted with addition of multiple pre-determined concentrations of Sn or SnS. If possible, determination of the tin-containing species in the electrolyte would also be beneficial in forming reasonable hypotheses as to how those species are affect-

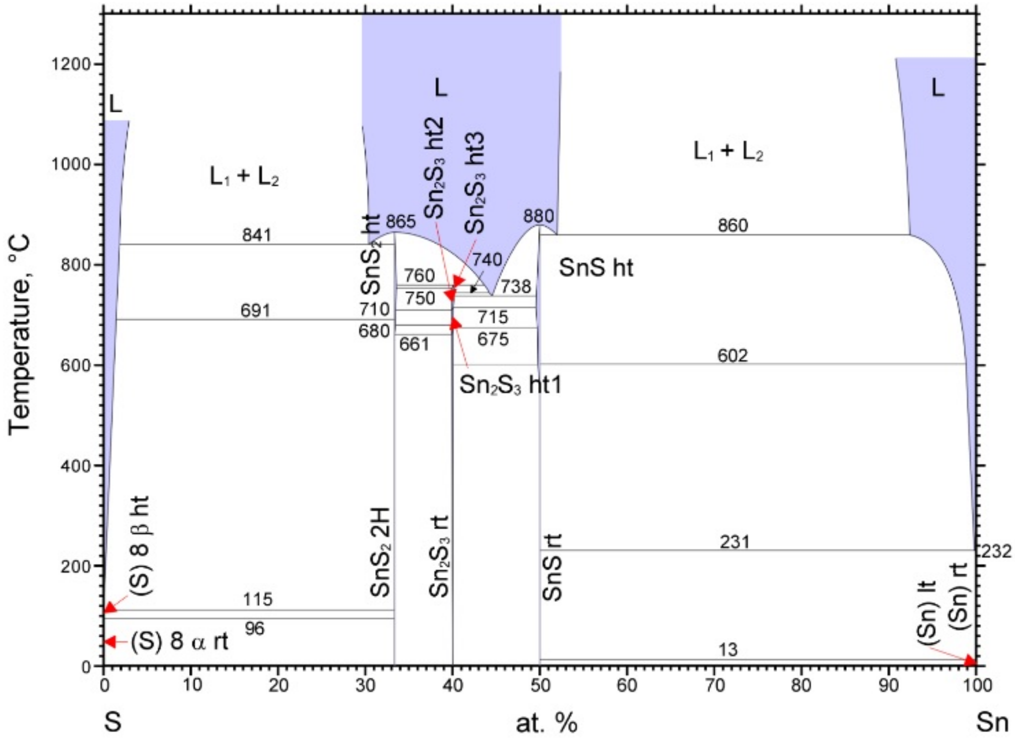

© ASM International 2006. Diagram No. 902053

Figure 4-10: Sn-S phase diagram [30]

ing the electronic character of the melt.

To determine whether or not the tin in the $Cu_{0.90}Sn_{0.10}$ electrode affected the results of the faradaic efficiency experiments, experiments should be conducted with another electrode, perhaps another liquid alloy or a second Cu electrode.

4.4 Effect of BaS Content on the Electronic Behavior of the Electrolyte

Changing the BaS content in the electrolyte is accompanied by a change in electronic behavior, and thus the BaS content may affect the premise upon which our previous arguments have been built upon: namely, that our electrolyte has semiconductive behavior. Studying the change in t_e and conductance with temperature as BaS content is adjusted is instructive in ascertaining whether the electrolytes in this study behave

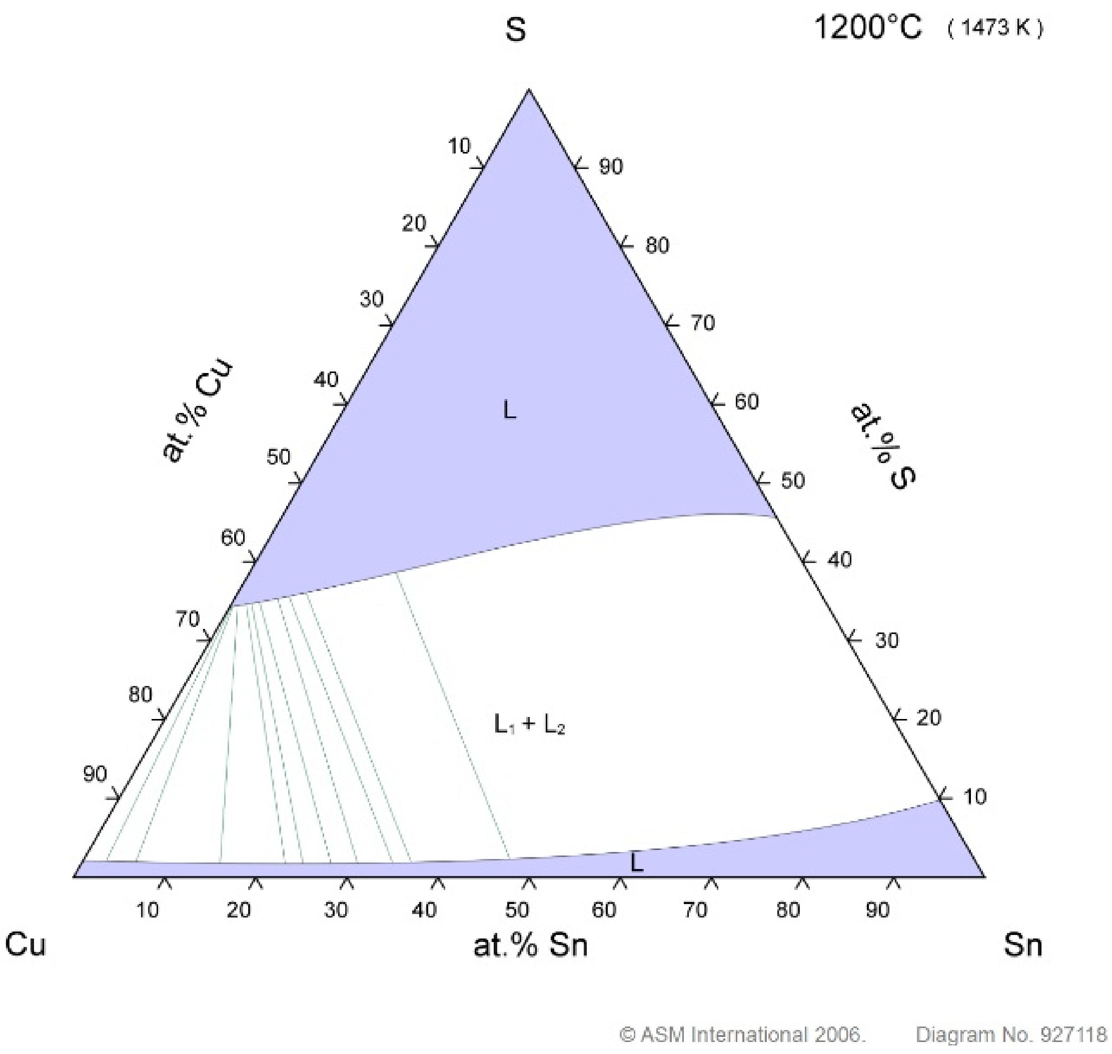

Figure 4-11: Isothermal section of the Cu-Sn-S ternary phase diagram at 1200°C [31]

as semiconductors or not.

Figure 3-6 shows a decrease in t_e as the electrolyte composition becomes more BaS-rich. This behavior is intuitive, as BaS is a semiconductor with a band gap of 3.7 eV in the solid-state [26] and an electronic conductivity of 10^{-3} Ω^{-1}cm^{-1} [18] at 1200K as compared to Cu_2S, which has a band gap of 1.2 eV in the solid-state [24] and an electronic conductivity of 20 Ω^{-1}cm^{-1} at 1200K [4]. While the band structures of these two materials are unknown in the liquid state, it can be inferred that by adding BaS to Cu_2S, the electronic conductivity of the mixture should be less than that of Cu_2S, even at high temperatures.

The variation across electrolyte composition of the change of conductance with temperature (Table 3.5) also supports that adding BaS makes the electrolyte behave less like a semiconductor. The conductivity decreased with increased temperature at the fastest rates for the most BaS-rich compositions and increased with increasing temperature at more Cu_2S-rich compositions.

The electronic transference numbers of a $(Cu_2S)_{0.73}(BaS)_{0.27}$ with a low purity of Cu_2S increase with increasing temperature, as presented in Table 3.1. This agrees with the theory that the molten semiconductors will lose short-range order and have a tendency to behave as a metal with increasing temperature, exhibiting higher electronic conductivity.

The electronic transference numbers of a $(Cu_2S)_{0.73}(BaS)_{0.27}$ with high purity Cu_2S, however, decrease with increasing temperature, as presented in Table 3.1. The conductance of this electrolyte increases with increasing temperature, like a semiconductor, but the change in t_e with temperature does not agree with the theory that semiconductors metallize and lose short-range order with increasing temperature.

In this study, all electrolytes with a higher BaS content exhibited the same decrease in t_e with increasing temperature, as presented in Figures 3-6 and 3-7. This, however, is less surprising, as the conductance of these electrolytes decreased with increasing temperature, which does not indicate a semiconductive behavior.

We have two possible explanations for a decrease in t_e with temperature. The first explanation is the simplest: the electrolyte may not be semiconductive, so increasing in temperature would decrease the mobility of the electrons or holes and would not generate more carriers. The second explanation is that ionic conductivity is thermally activated, so ionic conductivity should increase with temperature. If the electrolyte actually is semiconductive, a decrease in t_e may be because the barrier to ionic conduction is lower than that of electron or hole conduction, allowing the change in ionic conductivity to dominate the change in t_e with temperature.

4.4.1 Proposed Future Work

In order to understand more about the fundamental behavior of the electrolyte, it would be beneficial to conduct a study on the structure of the electrolyte across the composition range. Studying the change in kinematic viscosity with temperature could indicate whether or not aftermelting occurs, using the methods described by Regel [15].

It would also be beneficial to be able to distinguish between the contributions of ionic and electronic conductivity, for which three studies are proposed. The first is to measure the ionic and electronic conductivities separately using the residual potential method described by Yokota [11]. The second is to use radioactive tracers to determine ionic diffusion. The third is to study the dielectric constant as a function of frequency, as ions and electrons respond to electrical signals at different rates.

Chapter 5

Conclusion

Electronic transference numbers (t_e) have been estimated using two methods, stepped potential chronoamperometry and faradaic efficiency. The methods yield significantly different results, with stepped potential chronoamperometry estimating t_e between 0.73 and 0.85 for the same electrolyte for which faradaic efficiency experiments estimate t_e between 0.12 and 0.34, depending on the applied voltage. This result has multiple possible causes, but it is difficult to determine with certainty the extent of their effects.

The three explanations proposed in this work center around the role of the work functions of the electrode material used, the role of the driving force for Cu to alloy into Sn in faradaic efficiency experiments, and the role of Sn impurities in the electrolyte.

If we assume that the electrolyte does not itself change drastically with applied voltage, then we can use applied voltage to probe the influence of the work functions of the electrodes at the electrode-electrolyte interface. Borrowing the Schottky barrier concept from solid-state semiconductor physics, we can hypothesize that the difference in the Fermi levels between the electrodes and the electrolyte could have a significant effect on the barrier to electronic conduction. As the difference between the work function of Cu (used in faradaic efficiency experiments) and the electron affinity of Cu_2S is larger than that between graphite (used in stepped potential chronoamperometry experiments) and Cu_2S, we would anticipate electronic conduction to be easier in stepped potential chronoamperometry experiments, causing t_e to be greater in stepped potential chronoamperometry measurements. In fact, a simple mathematical model suggests that the 0.3 eV difference between the work functions of Cu and graphite alone would cause an electronic current more than 17 times greater when graphite is used. One would then anticipate t_e from stepped potential chronoamperometry experiments to be as high as 0.70 when t_e from faradaic efficiency experiments is only 0.12. This former value slightly underestimates the values determined experimentally by stepped potential chronoamperometry, but clearly illustrates the impact of the electrode work function on measurements.

Another aspect of electrode choice is the driving force for ionic transport through the electrolyte when alloying is energetically favorable. There is an additional driving force for Cu to alloy into Sn that is present in faradaic efficiency experiments but not in stepped potential chronoamperometry experiments. However, is not expected to have an effect as drastic as the electrode work function. This additional driving force is expected to represent an error of only $\sim$3% on t_e.

In addition to considering the impact of electrode choice, we must consider how the electrolyte itself may differ between experiments and impact the results. In particular, we are concerned with the tin impurities in the electrolyte, an increase of which seems to be accompanied by a decrease in t_e. This can be seen by comparing t_e estimated using stepped potential chronoamperometry for electrolytes prepared with high purity and with low purity Cu_2S. Table 3.1 shows that when a high purity Cu_2S is used, t_e ranges from 0.92 to 0.95 and decreases with increasing temperature. When a low purity Cu_2S is used, not only does t_e range from lower values of 0.65 to 0.85, but it also increases with increasing temperature. Tin is also added to the electrolyte in faradaic efficiency experiments in small amounts, as can be seen from comparing the composition of the electrolyte when Cu-Sn alloys of varying Sn content are used, as shown in Figure A-1. Tin originating from the $Cu_{0.90}Sn_{0.10}$ electrodes used could change the composition and electronic behavior of the electrolyte, reducing t_e, although the precise nature of the tin-containing species and its effect on the electronic structure of the electrolyte remain unclear.

The electronic structure of the electrolyte and its evolution as a function of BaS content remains unknown, but the electronic transference number estimations made using stepped potential chronoamperometry, shown in Figures 3-6 and 3-7, along with the conductance measurements from EIS, shown in Table 3.5, indicate that the addition of BaS may make the electrolyte behave less like a semiconductor. In addition, the temperature dependence of t_e from those experiments, which show that t_e decreases with increasing temperature for most of the compositions studied, do not agree with the hypothesized metallization behavior.

These results suggest that measuring the true transport properties of the electrolyte is not simple. The experimental apparatus has a significant effect on the measurements made, and it must be taken into consideration. In order to estimate the transport properties of the electrolyte used for electrochemical applications, an effort should be made to use the same electrodes that would be present during electrolysis, so that while the true transport properties cannot be measured, at least the transport properties under the relevant experimental conditions can be determined.

It is interesting to note, however, that because the electrode choice appears to significantly affect t_e and t_i, the faradaic efficiency of electrolysis could be improved through electrode choice, rather than by changing the electrolyte composition. It is certainly worth future study. This work also motivates further research into the physical and electronic structure of molten sulfides that have semiconductive behavior, as well as how these structures evolve as a function of composition.

Appendix A

Stability of Electrolyte and Cathode in Faradaic Effiency Experiments

The stability of liquid Cu-Sn of three compositions($Cu_{0.85}Sn_{0.15}$, $Cu_{0.90}Sn_{0.10}$, and $Cu_{0.95}Sn_{0.05}$)and the electrolyte together is tested. $Cu_{0.75}Sn_{0.25}$ inclusions, as shown in Figure A-1, were found in the electrolyte. The $Cu_{0.75}Sn_{0.25}$ inclusions are larger and more prevalent in the electrolyte with increasing copper content in the Cu-Sn alloy. There are two distinct sulfide phases in the electrolyte, a lighter barium-rich phase with a composition of $Cu_{0.465}Ba_{0.163}Sn_{0.001}S_{0.371}$ and a darker copper-rich phase with a composition of $Cu_{0.546}Ba_{0.092}Sn_{0.001}S_{0.361}$. The compositions of the electrolyte phases do not vary with the composition of the copper-tin alloy.

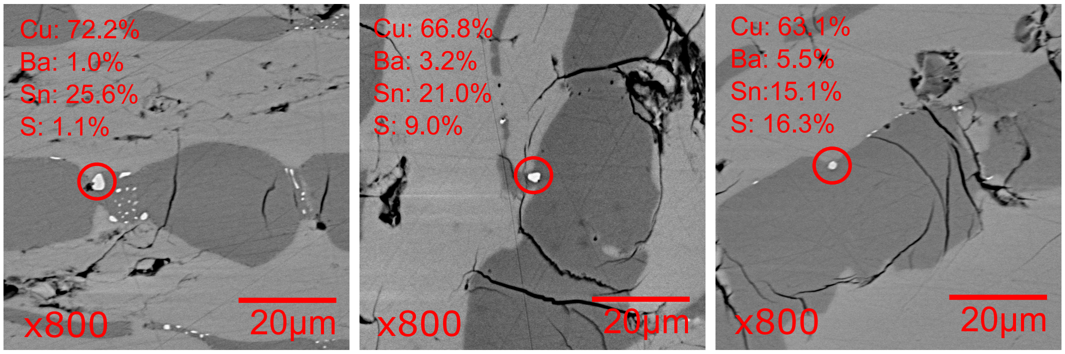

(a) Electrolyte with $Cu_{0.85}Sn_{0.15}$

(b) Electrolyte with $Cu_{0.90}Sn_{0.10}$

(c) Electrolyte with $Cu_{0.95}Sn_{0.05}$

Figure A-1: Electrolytes after blank experiment with Cu-Sn cathodes of 3 different compositions at 950°C

The copper-tin alloy solidified into copper-rich α dendrites and $Cu_{0.75}Sn_{0.25}$, as shown in the Cu-Sn phase diagram shown in Figure 2-7. There are also sulfide inclusions incorporated into the Cu-Sn. These inclusions vary in size and composition with cathode composition. When $Cu_{0.85}Sn_{0.15}$ and $Cu_{0.90}Sn_{0.10}$ are the cathodes only Cu_2S is found, as shown in Figure A-2a and Figure A-2b, respectively. Cu_2S, Cu_2S-BaS of the same composition as the electrolyte, and $Ba_{0.29}Sn_{0.26}O_{0.45}$ are found in the cathode when $Cu_{0.95}Sn_{0.05}$ is used, as shown in Figure A-2c. The sulfide inclusions increased in size as the copper content of the cathode increased.

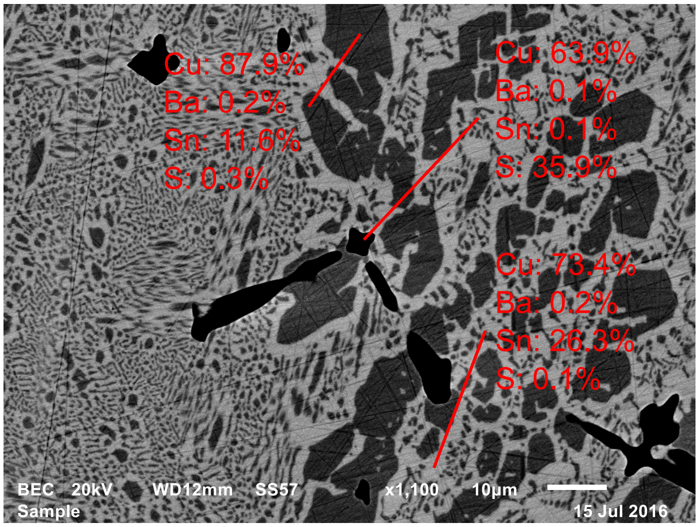

(a) $Cu_{0.85}Sn_{0.15}$

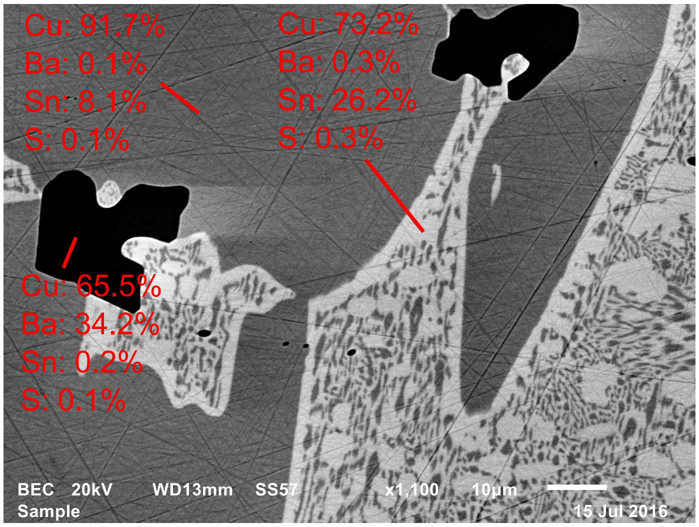

(b) $Cu_{0.90}Sn_{0.10}$

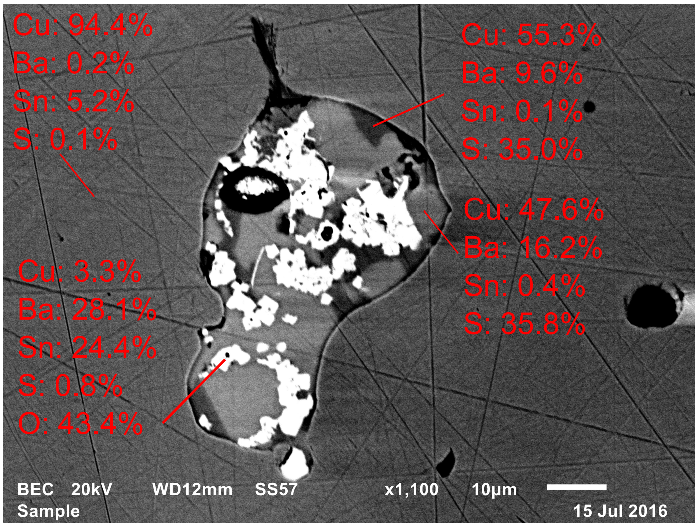

(c) $Cu_{0.95}Sn_{0.05}$

Figure A-2: Sulfide inclusions in Cu-Sn cathodes of 3 different compositions after blank experiment at 950°C

Appendix B

Determination of Copper-Tin Electrode Composition

The blank copper-tin electrode composition was determined through multiple methods, namely external analysis with direct current plasma emission spectroscopy (DCPES), estimating the first α phase to solidify, and using image analysis and either averaging measured α values, discretizing the α phase into two or three compositions, or estimating the α phase continuously.

A maximum copper content of 95.96 at% was found. Making the assumption that the quench was sufficiently rapid so as to disallow solute redistribution, the 95.96 at% Cu is taken to be the first α to solidify from the liquid electrode, corresponding with an initial copper content of 88.02 at% solidifying at 872°C.

Using an image analysis method, the composition is estimated by finding the average α composition, the average inter-dendritic composition (composed of $Cu_{0.75}Sn_{0.25}$ and α), and the area fraction of each phase. The average α copper content is 93.32 at%, and the average inter-dendritic composition is 83.98 at%. The area fraction of the α phase determined from the optical image, as shown in Figure B-1a, is 0.683 and that from the WDS image, as shown in Figure B-1c, is 0.667. The calculated composition from the optical and WDS images are 90.36 at% and 90.21 at%, respectively.

In order to try to optimize the estimation of the copper-tin electrode composition, the α phase is discretized into two or three components to better weight the more and less copper-rich regions. The calculated compositions are 90.28 at% and 90.45 at% when α is discretized into two or three divisions, respectively. The average composition for each division, the area fraction for each, and the final composition are reported in Table B.1.

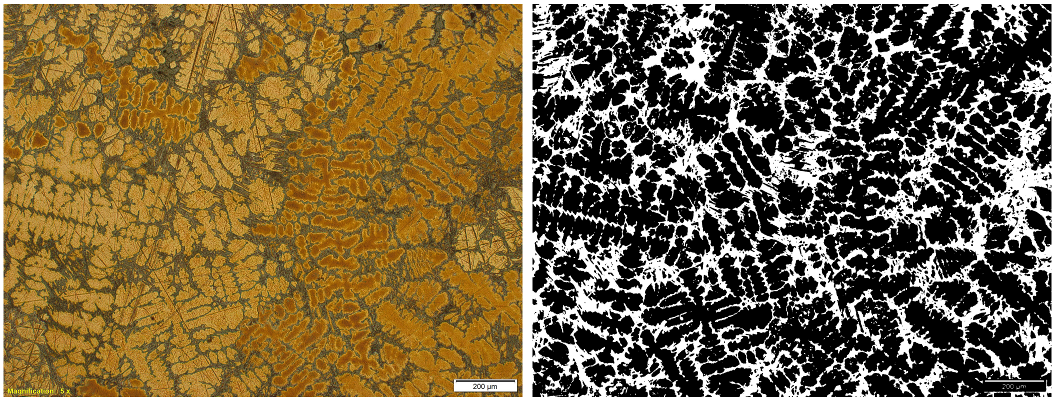

(a) 5x optical image of etched sample (b) ImageJ output from optical image

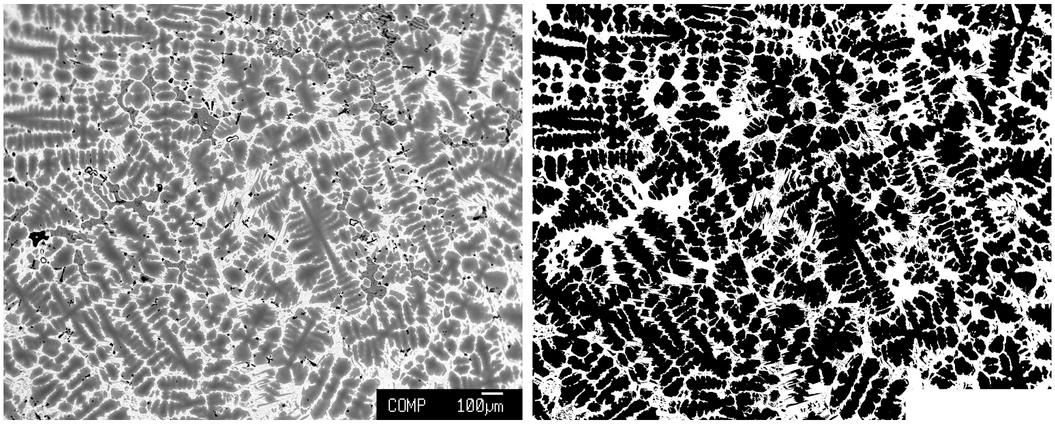

(c) Backscattered electron image from electron microprobe (d) ImageJ output from electron microprobe

Figure B-1: Image processing of copper-tin electrode from a blank experiment at 950°C

The composition of the α dendrites was also estimated by taking a continuous range of composition and matching it to the pixel intensity histogram, which is shown in Figure B-2. The darkest pixels are matched with the most copper-rich composition expected to be in the α phase. This composition is estimated with either the most copper-rich composition found in the line scans or the first α expected to solidify based on the phase diagram. The lightest pixels in the histogram peaks associated

Table B.1: Compositional estimates using subdivided α phases for the copper-tin electrode from a blank experiment at 950°C

$\#\alpha$ Divisions	Phases		Area Fraction	Phase Composition (at %Cu)		Total Composition (at %Cu)
2	α	Dark	0.262	94.61	93.41	90.28
		Light	0.406	92.63		
	Interdendritic		0.332	83.98		
3	α	Dark	0.154	95.46	93.65	90.44
		Medium	0.238	94.09		
		Light	0.276	92.27		
	Interdendritic		0.332	83.98		

with the α phase are matched with the least copper-rich dendritic composition found, the eutectic composition at 798°C, and the most tin-rich α composition from the phase diagram. The interdendritic phases are separated into Cu_3Sn and the most tin-rich α composition from the phase diagram by separating the lighter histogram peak into two sections. The calculated estimates for the copper-tin electrode are included in Table B.2.

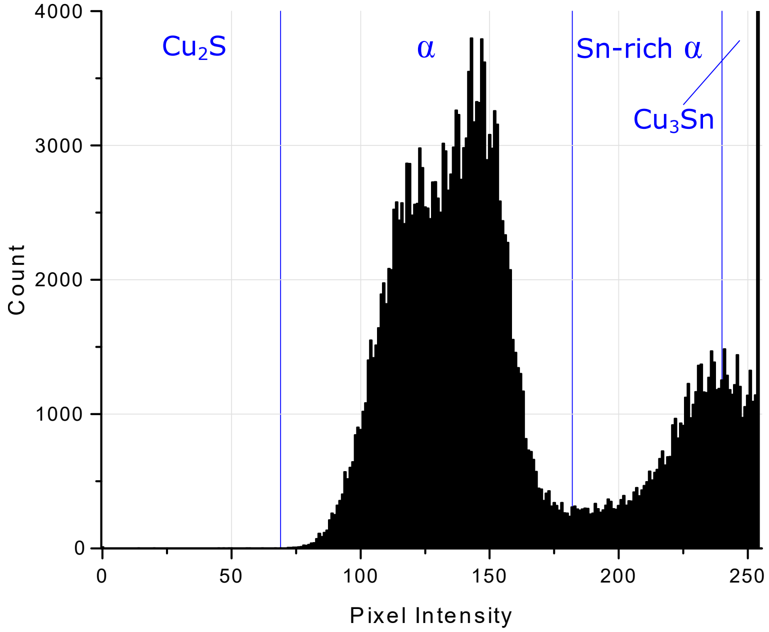

Figure B-2: Pixel intensity histogram from the copper-tin electrode from a blank experiment without application of voltage at 950°C

External DCPES analysis of the copper-tin alloy by Luvak determines the copper, tin, barium, iron, nickel, lead, and zinc levels, and combustion infrared detection by

Table B.2: Compositional estimates using continuous α phase estimations for the copper-tin electrode from a blank experiment at 950°C

		Maximum α Copper Content (at%)	
		Phase Diagram Max	Max Measured
Minimum α Copper Content (at%)	Phase Diagram Min	90.27	89.89
	Eutectic	90.70	90.32
	Min Measured	90.29	89.91

Luvak determines the carbon content. These values are reported in Table B.3. The composition of the copper-tin electrode from this analysis is 89.80 at%.

Table B.3: Luvak analysis of copper-tin electrode from a blank experiment at 950°C

Element	at%
Copper	89.63
Tin	10.18
Carbon	0.04
Barium	0.14
Iron	0.004
Nickel	0.005
Lead	0.002
Zinc	0.0005

The composition estimates described above for the copper-tin electrode from a blank experiment are summarized in Table B.4. The worst estimate by far comes from the first α to solidify method. The best estimate comes from using a continuous composition range for α, particularly with the maximum value being from a measured value. The value chosen for the minimum can be either the minimum from the phase diagram and the minimum measured value, as both lead to a near-identical result. The other methods overestimate the copper content of the electrode slightly.

Table B.4: Summary of composition estimates for a copper-tin electrode from a blank experiment at 950°C

Method	Composition (at% Cu)
First α to Solidify	88.02
Averaged α	90.21
2 Divisions of α	90.28
3 Divisions of α	90.45
Continuous α from Phase Diagram Values	90.27
Continuous α from Measured Values	89.91
External Analysis	89.80

Appendix C

Energy Level Description from Solution Resistance

The solution resistance of the electrolyte decreases with temperature when a high purity Cu_2S is used, as presented in Table 3.4. This suggests that the electrolyte acts as a semiconductor. The relation between conductivity and temperature for extrinsic p-type semiconductors is given in Equation C.1. Figure C-1 shows the fit of the conductivity data to this relation. According to this data, the energy difference between the acceptor level and the valence band is 0.136 eV.

$$\sigma \propto \exp(\frac{-(E_c - E_d)}{kT}) \tag{C.1}$$

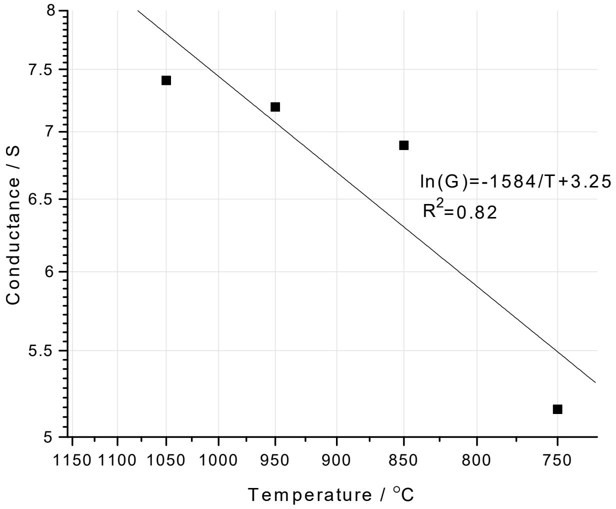

Figure C-1: Arrhenius relation between conductance and temperature for $(Cu_2S)_{0.73}(BaS)_{0.27}$ with high purity Cu_2S

Appendix D

Time Dependence of Solution Resistance

Time and temperature are coupled in stepped potential chronoamperometry measurements. Solution resistances measured throughout experimentation at 1000°C for $(Cu_2S)_{0.455}(BaS)_{0.545}$ with low purity Cu_2S are reported as a function of time in Figure D-1. Solution resistance increases as a function of time, and this could cloud the effect of temperature.

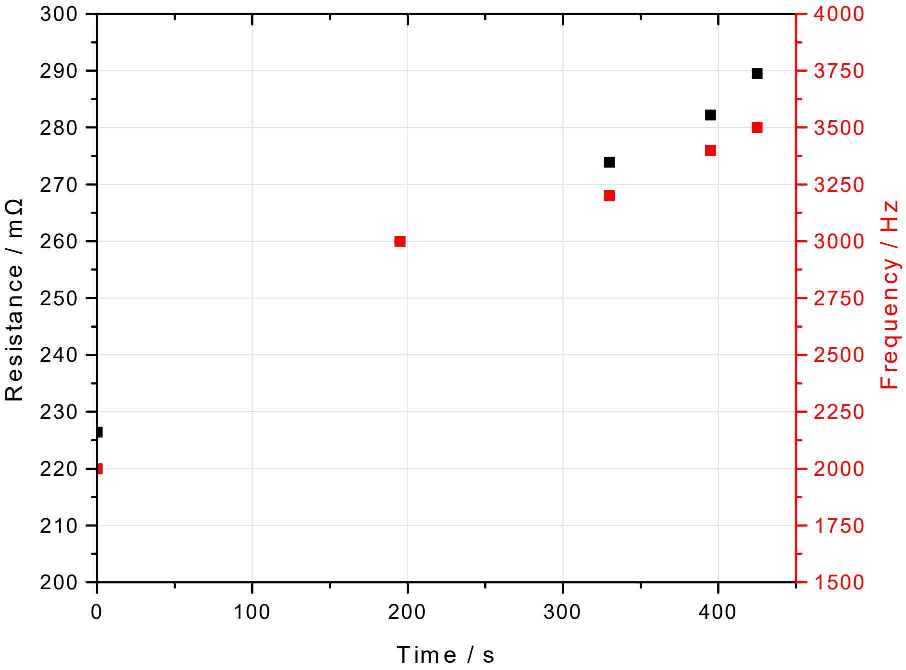

Figure D-1: Time dependence of the real component of impedance and frequency when the imaginary component of impedance is 0Ω for $(Cu_2S)_{0.455}(BaS)_{0.545}$ with low purity Cu_2S at 1000°C

Bibliography

[1] Samira Sokhanvaran, Sang-Kwon Lee, Guillaume Lambotte, and Antoine Allanore. Electrochemistry of molten Sulfides: copper extraction from BaS-Cu2S. *Journal of The Electrochemical Society*, 163(3):D115–D120, 2016.

[2] W. G. Davenport, M. King, M. Schlesinger, and A. K. Biswas. *Extractive metallurgy of copper.* Elsevier Science Ltd., Oxford, 4th edition, 2002.

[3] René Caldentey and Susana Mondschein. Policy model for the pollution control in the copper industry, including a model for the sulfuric acid market. *Operations Research*, 51(1):1–16, 2003.

[4] V. M. Glazov and A. S. Burkhanov. Physicochemical properties of copper and silver chalcogenides in the solid and liquid states. *Inorganic Materials*, 16(4):373–391, 1980.

[5] Naomi A. Fried, Kevin G. Rhoads, and Donald R. Sadoway. Transference number measurements of TiO2-BaO melts by stepped-potential chronoamperometry. *Electrochimica Acta*, 46(22):3351–3358, 2001.

[6] C. Tubant. Über Elektrizitätsleitung in festen kristallisierten Verbindungen. Zweite Mitteilung. Überführung un Wanderung der lonen in einheitlichen festen Elektrolyten. *Zeitschrift für anorganische und algemeine Chemie*, 115(1):105–126, 1921.

[7] Ling Yang, G. M. Pound, and G. Derge. Mechanism of electrical conduction in molten Cu2S-CuCl and mattes. *Journal of Metals*, 8:783–788, 1956.

[8] Hirohisa Endo, Makoto Yao, and Katsuhiko Ishida. Ionic conductivity and electronic properties of liquid Ag chalcogenides up to 1500 degrees C. *Journal of the Physical Society of Japan*, 48(1):235–237, 1980.

[9] Shin-ya Miyatani. On the polarization of silver sulfide. *Journal of the Physical Society of Japan*, 10(9):786–793, 1955.

[10] T. Usuki, K. Maruyama, and S. Tamaki. Electronic and ionic conductions in molten Tl-chalcogen systems. *Journal of Non-Crystalline Solids*, 156-158:752–755, 1993.

[11] Isaaki Yokota. On the theory of mixed conduction with special reference to the conduction in silver sulfide group semiconductors. *Journal of the Physical Society of Japan*, 16(11):2213–2223, 1961.

[12] E. A. Guggenheim. *Mixtures.* Oxford University Press, London, 1952.

[13] Norio Sato. *Electrochemistry at metal and semiconductor electrodes.* Elsevier, Amsterdam, 1998.

[14] J. E. Enderby and A. C. Barnes. Liquid semiconductors. *Reports on Progress in Physics*, 53:85–179, 1990.

[15] A. R. Regel, V. M. Glazov, and S. G. Kim. Structure defects in molten semiconductors (review). *Soviet Physics. Semiconductors*, 17(10):1105–1116, 1983.

[16] D. P. Belotskii and O. N. Manik. On the interrelation between parameters of certain thermoelectric materials and state diagrams. *Journal of Thermoelectricity*, 4:38–42, 2002.

[17] Byeong-Joo Lee, Bo Sundman, Sung Il Kim, and Kwang-Geun Chin. Thermodynamic calculations on the stability of Cu2S in low carbon steels. *ISIJ international*, 47(1):163–171, 2007.

[18] Walter Grattidge and Harold John. The electronic properties of barium sulfide. *Journal of Applied Physics*, 23(10):1145, 1952.

[19] H. Okamoto. Ba-S. In T. B. Massalski, editor, *Binary Alloy Phase Diagrams, Vol. 1*, pages 610–611. ASM International, 2nd edition, 1990.

[20] O. V. Andreev and N. N. Parshukov. The Cu2S-BaS system as a possible high-temperature superconductor. *Russian journal of inorganic chemistry*, 36(8):1190–1191, 1991.

[21] Safa O. Kasap. *Principles of Electrical Engineering Materials and Devices.* McGraw-Hill, Boston, 1st edition, 1997.

[22] Hans Lüth. *Solid surfaces, interfaces and thin films.* Springer-Verlag, London, 6 edition, 2015.

[23] S. B. L. Mathur. The thermionic work function of graphite-III, 1952.

[24] Guangming Liu, T. Schulmeyer, J. Brötz, A. Klein, and W. Jaegermann. Interface properties and band alignment of Cu2S/CdS thin film solar cells. *Thin Solid Films*, 431-432(03):477–482, 2003.

[25] Shigehiko Yamamoto. Work functions of binary compounds. *The Journal of Chemical Physics*, 60(10):4076, 1974.

[26] Mohammed Ameri, Keltouma Boudia, Abbes Rabhi, Samir Benaissa, Yarub Al-douri, Abdelmadjid Rais, and Djelloul Hachemane. FP-LMTO calculations of structural and electronic properties of alkaline-earth chalcogenides alloys AY : A = Ca , Sr , Ba ; Y = S. *Materials Sciences and Applications*, 3(December):861–871, 2012.

[27] Jae-Hyeok Shin, Chang-Seok Oh, Byeong-Joo Lee, and Dong Nyung Lee. Thermodynamic assessment of the Cu-Sn system. *Zeitschrift fuer Metallkunde*, 87(March):205–212, 1996.

[28] P. Oelhafen, R. Wahrenberg, and H. Stupp. Electronic structure of liquid transition metals studied by time resolved photoelectron spectroscopy. *J. Phys.: Condens. Matter*, 12:A9–A18, 2000.

[29] Allen J. Bard and Larry R. Faulkner. *Electrochemical Methods Fundmentals and Applications*. John Wiley & Sons, Inc., New York, 2nd edition, 2001.

[30] R. C. Sharma and Y. A. Chang. S-Sn. In T. B. Massalski, editor, *Binary Alloy Phase Diagrams, Vol. 3*, pages 3280–3283. ASM International, 2nd ed. edition, 1990.

[31] Y. A. Chang, J. P. Neumann, and U. V. Choundary. *Phase diagrams and thermodynamic properties of ternary copper-sulfur-metal systems*, volume 7. 1979.

[32] D. M. Chizhikov, A. V. Imenitov, and V. G. Finikov. Preservation of the short-range order structure during the melting of germanium, tin, and copper sulfides. *Fizika i Khimiya Obrabotki Materialov*, 6:96–97, 1971.

[33] Hyung Soon Im, Yoon Myung, Yong Jae Cho, Chang Hyun Kim, Han Sung Kim, Seung Hyuk Back, Chan Su Jung, Dong Myung Jang, Young Rok Lim, Jeunghee Park, and Jae-Pyoung Ahn. Facile phase and composition tuned synthesis of tin chalcogenide nanocrystals. *RSC Advances*, 3(26), 2013.